Statistical Combinations Studies in Search for Invisible Higgs decays in Vector Boson Fusion with ATLAS detector

A MANUSCRIPT
SUBMITTED IN PARTIAL FULFILLMENT OF
THE REQUIREMENTS FOR THE DEGREE OF
MASTER IN MATHEMATICAL PHYSICS

By
EL ABASSI ABDERRAZAQ

Jury composed of :

Pr.R.AHL Laamara	*Professor at CRMEF,Fes-Meknes*	President
Pr. E.H. Saidi	*Professor at FSR-UMV Rabat*	Examiner
Pr.M.Gouighri	*Professor at FSK-UIT Kenitra*	Supervisor
Pr.Y.Tayalati	*Professor at FSR-UMV Rabat*	Examiner
Pr.D.Benchekroun	*Professor at FSAC-UHII Casablanca*	Examiner

NOVEMBER 20, 2020

Acknowledgments

It is strange how sometimes the journey seems so long when you start it, but once on the finish line you get lost before turning back to see where you came from, what you went through and what you have achieved!

Writing this manuscript would have been impossible without the strong ambition and hard teleworking in this pandemic situation the world is going through and with emotional helps from important people.

First of all, I thanks Allah for giving me patience and strength to made it that far and I am so gretful for it. I thanks Pr.EL Hassan SAIDI lab head of High energy physics, modelling and simulation , and it's really honor to me to present my work in front of him

I am also grateful for the supervisor of my manuscript,PR.M. GOUIGHRI for great emotional help and presious advices and useful guides, and his insistence for greater good and professional work

and Special Thanks to Pr.Y.Tayalati and Pr.D.Benchekroun for accepting the invitaion to be a member of the Jury , and Am so much gretful for this opportunity to have them both among us

A special thanks to Loan Troung,Professor at Johannesburg University, for the amount of time she put for clarification and guides which helps on shaping the necessary background to better understand my task topic.and also I thanks the rest of Higgs invisible Team: Valerio Dao, Philipp Mogg and Amanda Steinhebel for the clarifications and the useful discussions

Most of all, I would like to thank my parents who have been there for me since the first day of my existence, during the ups and downs providing the emotional support along with my siblings and my friends

Table of Contents

List of Figures

5

List of Tables

Introduction

The Unification of Electromagnatic field by Maxwell, leads to new Fundamental prespective of understanding the Universe in term of unifying the Fundamental forces in one Master equation. even the non-consistency in mathematical structure in terms of unification, The thoeritcal expectations leads to enermous obervations and exprerimental agreements. One of the Fundamental basic aspect is The Standard Model of particle physics

The Standard Model explains the three fundamental forces except gravity, in elegant way via the notion of symmetries that governs the universe in one Master group $SU(3) \otimes SU(2) \otimes U(1)$, the $SU(3)$ describes the strong force between quarks and gluons mediated by the gluons, and $SU(2) \otimes U(1)$ describes the electroweak interaction between leptons and quarks, spontaneously broken at energy scale $O(100 GeV)$, by the Higgs field. In 2012 the ATLAS and CMS expirements at CERN observed a 125 GeV scalar particle that finally proves the expectations of the Standard Model. Not only that,it seems to be able to explain enormous body of expiremental data and vast number of results from all areas of particle physics.despite this success , the Standard Model is not the final theory , it cannot explains the origin neutrinos masses and has a quite a lot of parameters, and mostly doens't include gravity or a quantum theory of gravity and cannot explain the dark matter and dark Energy claimed by the astrophysical observations.

One of the few concrete leads that particle physicists currently have is that of dark matter. The existence of dark matter (DM) is supported by a variety of astrophysical measurements, ranging from the rotational speed of stars in galaxies, over precision measurements of the cosmic microwave background , to gravitational lensing measurements . However, the nature and properties of the DM remain largely unknown. Searches for particle DM are performed using different complementary approaches : the measurement of elastic scattering of DM by nuclei and electrons in a detector [23, 13, 2, 3, 18, 1] , the detection of Standard Model (SM) particles produced in the annihilations or decays of DM in the universe , the production of DM particles at colliders [6] , and the study of the effect of DM interactions on astrophysical systems . Another major unknown in the physics of our universe, beside the nature of DM, is the origin of its accelerating expansion . In the context of a homogeneous and isotropic universe, this implies the existence of a repulsive force, which causes the universe to expand at an accelerating rate . Assuming general relativity, one of the simplest explanation for this repulsive force is a new type of matter which mimics a constant energy density, thus dubbed dark energy (DE). The effect of DE on cosmological scales is studied by measuring the redshift-distance relation using supernovae, baryon acoustic oscillations, the matter power spectrum and the cosmic microwave background, as well as gravitational lensing .

The main subject of this manuscript is to consider the hypothesis that the DM is composed of a Weakly Interacting Massive Particle (WIMP) . These particles, denoted by the symbol χ throughout this manuscript, are stable over cosmological scales and are not detected directly by the detector but through their decay final states.To identify events with DM, additional

particle(s), X = jet, γ, W, Z,($t\bar{t}$, need to be produced in association with DM in a pp collision, in order to tag the event and detect the recoiling WIMPs as missing transverse momentum (with magnitude E_T^{miss}).

This manuscript is devided into two part, Theoretical part and Experimental part. each part with two chapters, Chapter 1 presents general overview of the standard model and it's limitations. The Second chapter outline one of the most important models that is favored by the LHC experiments (ATLAS and CMS), which explains the dark matter at quantum level, known as the Higgs portal model, Where SM Higgs boson act as a portal to the dark sector, and we end the second chapter with an overview of the ATLAS detector and it's tracking systems.The first chapter in the experimental part of this manuscripts we summarize the Vector Boson Fusion analysis for invisible Higgs decay into pair of WIMP, where we describe the strategy of the analysis and different backgrounds contributions and interpret the result as an excluasion limit of WIMP-nucluon cross section in the context of Higgs portal model. Finally in last chapter we report the results we obtained in the study of the Statistical Combination of invisible Higgs decay, by combining the results reported in each DM analysis and interpreting the result as the exclusion limit of the branching ratio of invisible Higgs decay in the phase space of WIMPs-nucluon cross section and WIMPs mass and compare it with different direct detection expiremets

Part I

Theoretical Framework

Chapter 1

The Standard Model of Particle Physics

Quantum Field Theory [22] is a very successful framework for description of relativistic interactions of Quantum Fields in a Perturbative manner and provides strong predictions in many areas of physics , from condsensed matter physics to the standard model of high energy Physics.

The main subject of this chapter is to give the theoretical description of the SM, the classifications of the elementary particles and the forces that governs their interactions, and we precede with Gauge description of the theory and the fermionic sector and the higgs mechanism in Weinberg-Salam electroweak theory, and we end the chapter with Higgs production modes at LHC

1.1 Structure of Matter at high energies

According to current experimental knowledge and phenomenological observations at accessible energies, the elementary particles of the universe are of 2 types: fermions,a fundamental particles making atoms of known matter and bosons a gauge quanta mediating particles interactions.
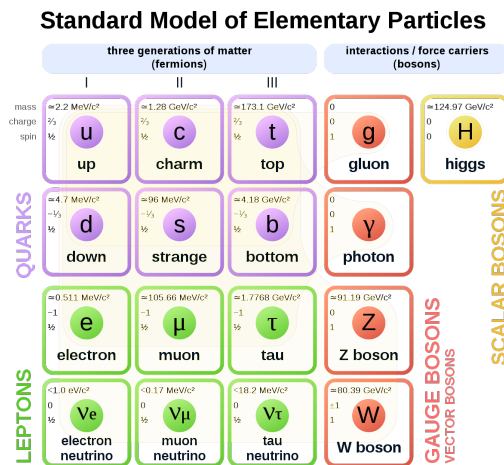
Figure 1.1: Classification of Standard Model Particles

The SM classifies all type of known matter particles into three generations of leptons and quarks Figure 1.1 and the gauge quanta($W^{\pm}, Z, \gamma, g$) that mediates their interactions, and including Higgs field(H) responsible for the masses and Electroweak symmetry breaking :

The SM is based on the assumption that the matter in the universe (quarks and leptons) consists of fermionic fields. These fields are quantized , which implies that their excitations can be thought of as particles.Futhermore this fields are invariant under a local transformations what so-called gauge transformations, the gauge group of the SM is denoted as :

$$G_{SM} = SU(3)_C \otimes SU(2)_L \otimes U(1)_Y$$

The SU(3) is the gauge group of strong interactions or what so-called Quantum Chromo-dynamics.describes the interactions between quarks and gluons. SU(3) is non-Abelian, which implies that the gluons self-interact. In the case of gluons, this leads to an effect called confinement, where no object which is charged under the strong interaction (colored) can exist independently. Instead, they always form bound states (hadrons). If a colored object is isolated, it quickly becomes energetically favorable to produce new quark-antiquark pairs, creating new hadrons. When a quark or gluon is produced in a high-energy collision, it typically results in a shower of hadrons (a jet).

The SU(2) symmetry. This has 3 generators, corresponding to 3 gauge fields. In practice, these SU(2) gauge fields mix with the U(1) component of the SM. but the end result is three vector bosons corresponding to the weak interaction ($W^{\pm}$ and Z) and one corresponding to the electromagnetic interaction (γ, the photon). Because of this unification, the two interactions are together referred to as the electroweak interaction. SU(2) is also non-Abelian, but since the W and Z are massive, this self-interaction doesn't result in confinement like QCD does. The weak gauge fields only interact with the left-handed chiral component of the fermion fields in the SM (the right-handed components are not charged under the weak interaction). The left-handed fermions are SU(2) doublets.

1.2 The Minimal Standard Model

The underlying success of QED leads to further breakthroughs to more generalised field theories by the investigation of large group symmetries than U(1) of Maxwell field theory. the Yang-Mills field theories was the most successful one and most renormalised gauge theories (QCD AND EW theory) to be agreed with experimental data.

The phenomenological description of the SM is maped in a lagrangian density formalism , in very elegant and more generalised fundamental manner:

$$\mathcal{L}_{SM} = \mathcal{L}_{Gauge} + \mathcal{L}_{Fermions} + \mathcal{L}_{Yukawa} + \mathcal{L}_{Higgs} \tag{1.1}$$

$\mathcal{L}_{Gauge}, \mathcal{L}_{Higgs}$ describes the kinematics and dynamic interactions of the gauge fields and their interaction with the Higgs Fields. $\mathcal{L}_{Fermions}, \mathcal{L}_{Yukawa}$ describes the kinematics of fermions and their interactions with the gauge fields, and interactions between Fermions and Higgs field through Yukawa coupling.

1.2.1 The Standard Model of Electroweak Interactions

EW Theory is one of the renormalised Yang-Mills theories to be agreed with experimental data, In this section we summerize the EW Theory sector and it's symmetry breaking.

1.2.1.1 Gauge Sector

The SU(2) has 3 generators associated with 3 gauge bosons[1] $(W_\mu^1, W_\mu^2, W_\mu^3)$. and U(1) has only one gauge boson (B_μ). The dynamic of this gauge field is described by the following lagrangian density:

$$\mathcal{L}_{Gauge} = -\frac{1}{4}\mathcal{W}_{\mu\nu}^a \mathcal{W}_a^{\mu\nu} - \frac{1}{4}\mathcal{B}_{\mu\nu}\mathcal{B}^{\mu\nu} \tag{1.2}$$

Where The Tensor Field strength for each gauge boson is giving by

$$\mathcal{W}_{\mu\nu}^a = \partial_\mu W_\nu^a - \partial_\nu W_\mu^a + g_2 \varepsilon^{abc} W_\mu^b W_\nu^c \tag{1.3}$$
$$\mathcal{B}_{\mu\nu} = \partial_\mu B_\nu - \partial_\nu B_\mu$$

With g_2 and ε^{abc} are respectively the SU(2) coupling and structure constantes, and g_1 of U(1) coupling constante, The non-abelian nature of SU(2) implies the self-intercations between The W_μ^a bosons.

1.2.1.2 Fermions Sector

In the relativistic 4D space-time Dirac theory, each of the particles of the three families is associated with a 4-component spinor field Ψ under SO(1,3) symmetry. Moreover since in 4D space-time , a Dirac Spinor has two chiralities[2], left-handed and right-handed given by:

$$\psi_{L,R} = \frac{1}{2}\left(\mathbb{I} \pm \gamma_5\right)\Psi \tag{1.4}$$

Additionally, The left-handed fermions and anti-fermions forms respectively a fundamental and antifundamental representation of SU(2) which is $2, \overline{2}$ respectively, and The right-handed forms a trivial 1 representation. Hence the left-handed are doublets under isospin symmetry, and the righ-handed are singlets under isospin symmetry.

Left Handed and Righ Handed leptons:

$$\Psi_L^1 = \begin{pmatrix} \nu_e \\ e \end{pmatrix} \qquad \Psi_L^2 = \begin{pmatrix} \nu_\mu \\ \mu \end{pmatrix} \qquad \Psi_L^3 = \begin{pmatrix} \nu_\tau \\ \tau \end{pmatrix} \tag{1.5}$$

$$\tag{1.6}$$

$$\psi_R^1 = e_R \qquad\qquad \psi_R^2 = \mu_R \qquad\qquad \psi_R^3 = \tau_R$$

---

[1] in representation theory, gauge bosons are often represented as adjoint representation for special Unitary groups SU(N), which is : $N^2 - 1$

[2] Dirac spinors can be represented as 2D weyl spinors with a propriety called chiral spinors

Left Handed and Right Handed Quarks:

$$Q_L^1 = \begin{pmatrix} u \\ d \end{pmatrix} \qquad Q_L^2 = \begin{pmatrix} c \\ s \end{pmatrix} \qquad Q_L^3 = \begin{pmatrix} t \\ b \end{pmatrix} \qquad (1.7)$$

$$(1.8)$$

$$U_R^1 = u_R \qquad\qquad U_R^2 = c_R \qquad\qquad U_R^3 = t_R$$
$$D_R^1 = d_R \qquad\qquad D_R^2 = s_R \qquad\qquad D_R^3 = b_R$$

The Dirac field equation describes the kinematics and the statistics of fermions. this fermions can be coupled to YM fields of the SU(2), and the U(1) field like :

$$\mathcal{L}_{fermions} = i(\overline{\Psi_L^k}\slashed{D}\Psi_{L,k} + \overline{Q_L^k}\slashed{D}Q_{L,k} + \overline{\psi_R^k}\slashed{D}\psi_{R,k} + \overline{U_R^k}\slashed{D}U_{R,k} + \overline{D_R^k}\slashed{D}D_{R,k}) \quad (1.9)$$

Where, the covariant derivative from $SU(2) \otimes U(1)$ gauge transformation can be written as follows:

$$\mathcal{D}_\mu = \partial_\mu - ig_2\frac{\sigma_a}{2}W_\mu^a - ig_1\frac{Y}{2}B_\mu \tag{1.10}$$

Where, σ^a(pauli matrices), Y are respectively the generators of SU(2) and U(1) (Hypercharge), and g_1, g_2 are respectively the coupling cte of U(1) and SU(2). The SU(2) isospin symmetry act only on left-Handed fermions, therefore we can express the covariant derivative actions as follows:

$$\mathcal{D}_\mu^L = \partial_\mu - ig_2\frac{\sigma_a}{2}W_\mu^a - ig_1\frac{Y}{2}B_\mu \tag{1.11}$$

$$\mathcal{D}_\mu^R = \partial_\mu - ig_1\frac{Y}{2}B_\mu \tag{1.12}$$

The lagrangian of the gauge and fermionic sector have no mass term, due to the gauge invariance . and that where the idea of spontaneous symmetry breaking in the SM comes in, A mechanism in which is the masses can be generated via the breaking $SU(2)_L \otimes U(1)_Y \to U(1)_{em}$.

1.2.1.3 Symmetry Breaking and Higgs Mechanism

In nature, a variety of beautiful and elegant symmetries surrounds us [22]. However,there are also many examples of symmetries in nature that are broken. Rather than put explicit symmetry-breaking terms into the Hamiltonian by hand, which seems artificial and unappealing, we would like to break these symmetries in a way such that the equations retain their symmetry. Nature seems to realize this by exploiting the mechanism of spontaneous symmetry breaking; that is, the Hamiltonian is invariant under some symmetry, but the symmetry is broken because the vacuum state of the Hamiltonian is not invariant.

The field that responsible for symmetry breaking is the main part of the Electroweak lagrangain, is giving by :

$$\mathcal{L}_{Higgs} = (\mathcal{D}_\mu \Phi)^\dagger (\mathcal{D}^\mu \Phi) - \mu^2 \Phi^\dagger \Phi - \lambda (\Phi^\dagger \Phi)^2 \tag{1.13}$$

Where Φ is complex scalar field. and an isospin doublet under SU(2), with charge $(I_3 = \frac{1}{2}, Y = +1)$:

$$\Phi = \begin{pmatrix} \phi^+ \\ \phi^0 \end{pmatrix} \tag{1.14}$$

The symmetry breaking of $SU(2) \otimes U(1)$ is achieved by investigating the parameters (μ, λ) of the potential:

$$V(\Phi) = \mu^2 \Phi^\dagger \Phi + \lambda (\Phi^\dagger \Phi)^2 \tag{1.15}$$

The $SU(2)_L \otimes U(1)_Y$ symmetry is spontaneously broken down to $U(1)_{em}$. For $\lambda > 0$, this corresponds to considering $\mu^2 < 0$ in order to have a non zero vacuum $\langle \Phi \rangle = 0$. In fact, we have an infinitely degenerate vacuum given by the circle Fig 1.2

$$\langle \Phi^\dagger \Phi \rangle = -\frac{\mu^2}{2\lambda} \tag{1.16}$$

To break spontaneously the $SU(2) \otimes U(1)$ symmetry down to $U(1)_{em}$, we have to choose the vacuum as

$$\langle \Phi \rangle = \frac{\sqrt{2}}{2} \begin{pmatrix} 0 \\ \nu \end{pmatrix} \tag{1.17}$$
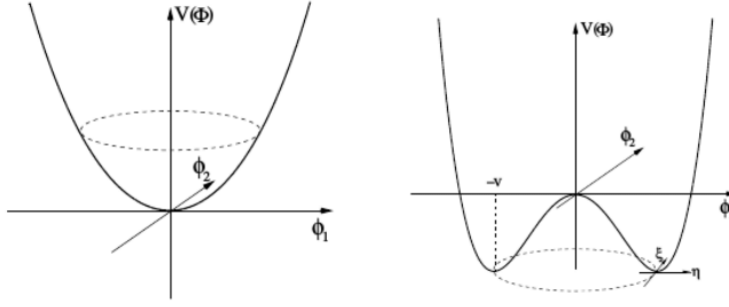
Figure 1.2: the potential of the scalar field , the left side represent the minimum with $\mu^2 > 0$, the right side represent the minimas with $\mu^2 < 0$

With $\nu^2 = \frac{\mu^2}{\lambda}$. if we power expand around the vaccum toghter with Kibble parametrisation, we can write like

$$\Phi = \frac{\sqrt{2}}{2} e^{i\theta_a \sigma^a} \begin{pmatrix} 0 \\ \nu + H \end{pmatrix} \tag{1.18}$$

With θ_a are Goldstone bosons.using the gauge invariance to kill the decoupled Goldstone bosons, we end up with:

$$\Phi = \frac{\sqrt{2}}{2} \begin{pmatrix} 0 \\ \nu + H \end{pmatrix} \tag{1.19}$$

It is straightforward to show that:

$$V(\Phi) = \frac{1}{2}\mu^2(\nu + H)^2 + \frac{\lambda}{4}(\nu + H)^4 \tag{1.20}$$

$$= \frac{\mu^2}{4}\nu^2 + \frac{\mu^2}{4}H^2 + \frac{\mu^2}{2}\nu H + \frac{\lambda}{4}H^4 + \lambda\nu H^3 + \frac{3}{2}\lambda\nu^2 H^2 + \lambda\nu^3 H + \frac{\lambda\nu^4}{4}$$

Using the definition of ν^2, we end up with

$$V(H) = -\mu^2 H^2 + \lambda\nu H^3 + \frac{\lambda}{4}H^4 \tag{1.21}$$

This is the final Higgs potential after symmetry breaking, where the first term is the mass term, the second and the third terms represent respectively the trilinear and quadratic self-interactions of the Higgs.The mass of the Higgs is given by:

$$M_H = \sqrt{\lambda\nu} = \sqrt{-\mu^2} \tag{1.22}$$

15

The main principal of the Higgs phenomena, is to give mass to the gauge bosons (Z,W). and the mass for the fermions .

The gauge bosons gains their mass via the dynamic part of $\mathcal{L}_{Higgs}$.we can expand the covaraint derivative on Φ like :

$$\begin{aligned}
\mathcal{D}_\mu \Phi &= (\partial_\mu - ig'\frac{\sigma_a}{2}W_\mu - ig\frac{Y}{2}B_\mu)\Phi \\
&= (\partial_\mu - iS_\mu)\Phi
\end{aligned} \tag{1.23}$$

Where the gauge matrix S_μ is giving by:

$$iS_\mu = \frac{1}{2}\begin{pmatrix} gB_\mu + g'W_\mu^3 & g'(W_\mu^1 - iW_\mu^2) \\ g'(W_\mu^1 + iW_\mu^2) & gB_\mu - g'W_\mu^3 \end{pmatrix} \tag{1.24}$$

Using the orthogonal transformation of $O(2)$, or what so-called Weinberg transformation:

$$\begin{pmatrix} W_\mu^3 \\ B_\mu \end{pmatrix} = \begin{pmatrix} cos(\theta_w) & -sin(\theta_w) \\ sin(\theta_w) & cos(\theta_w) \end{pmatrix}\begin{pmatrix} Z_\mu \\ A_\mu \end{pmatrix} \tag{1.25}$$

Setting

$$sin(\theta_w) = \frac{g'}{\sqrt{g'+g}} \qquad cos(\theta_w) = \frac{g}{\sqrt{g+g'}} \tag{1.26}$$

$$W_\mu^\pm = \frac{1}{\sqrt{2}}(W_\mu^1 \pm iW_\mu^2) \tag{1.27}$$

Therefore, we can write the Dynamic expression, straightforwardly like

$$\begin{aligned}
(\mathcal{D}_\mu\Phi)^\dagger(\mathcal{D}^\mu\Phi) &= \frac{1}{2}\partial_\mu H\partial^\mu H + \frac{1}{4}g'W_\mu^+ W^{-\mu}(\nu + H)^2 \\
&+ \frac{1}{8}(g'^2 + g^2)Z_\mu Z^\mu(\nu + H)^2
\end{aligned} \tag{1.28}$$

Finally, the expression of $\mathcal{L}_{Higgs}$

$$\begin{aligned}
\mathcal{L}_{Higgs} &= \frac{1}{2}\partial_\mu H\partial^\mu H - 2\lambda\nu H^2 - \lambda\nu H^3 - \frac{\lambda}{4}H^4 + \frac{1}{4}\nu^2 g'^2 W_\mu^+ W^{-\mu} \\
&+ \frac{1}{4}g'^2 W_\mu^+ W^{-\mu}H^2 + \frac{1}{2}\nu g'^2 W_\mu^+ W^{-\mu}H + \frac{1}{8}\nu^2(g'^2 + g^2)Z_\mu Z^\mu \\
&+ \frac{1}{8}(g'^2 + g^2)Z_\mu Z^\mu H^2 + \frac{1}{4}\nu Z_\mu Z^\mu H
\end{aligned} \tag{1.29}$$

The masses of the gauge bosons

$$M_Z^2 = \frac{1}{4}(g'^2 + g^2)\nu^2 \qquad M_W^2 = \frac{1}{2}g'^2\nu^2 \qquad M_A^2 = 0 \qquad (1.30)$$

After generting the masses for the Gauge bosons (W,Z) via the Dynamic coupling.The phenomena can generate the masses for the fermions via Yukawa coupling.

1.2.1.4 Yukawa Sector

The mass terms of the fermions is exclauded by the gauge invariance, due to the fact that the left-Handed and the right-handed are transforms differently under isospin symmetry, therfore the Higgs mechanism is applied to the fermions via Yukawa interactions giving by the lagrangian :

$$\begin{aligned}
\mathcal{L}_{Yukawa} = &-\lambda_i^{lep}\overline{\Psi}_L^i \Phi \psi_R^i + h.c \\
&- \Lambda_{ij}^{down}\overline{Q}_L^i \Phi D_R^j - \Lambda_{ij}^{up}\overline{Q}_L^i \Phi U_R^j + h.c
\end{aligned} \qquad (1.31)$$

Where λ_i are the coupling constant between the leptons and the Higgs , and the $\Lambda_{ij}^{up}, \Lambda_{ij}^{down}$ are respectively the 3×3 coupling matrices of up and down quarks that cannot be diagonalize simultaneously .

Leptons :

$$\begin{aligned}
\mathcal{L}_{Yukawa}^{lep} = &-\frac{\sqrt{2}}{2}\lambda_1^e((\overline{\nu_{eL}} \quad \overline{e}_L)\begin{pmatrix} 0 \\ \nu + H \end{pmatrix})e_R \\
&- \frac{\sqrt{2}}{2}\lambda_2^\mu((\overline{\nu_{\mu L}} \quad \overline{\mu}_L)\begin{pmatrix} 0 \\ \nu + H \end{pmatrix})\mu_R \\
&- \frac{\sqrt{2}}{2}\lambda_3^\tau((\overline{\nu_{\tau L}} \quad \overline{\tau}_L)\begin{pmatrix} 0 \\ \nu + H \end{pmatrix})\tau_R \\
&+ h.c
\end{aligned} \qquad (1.32)$$

The masses of the three leptons is related to their coupling with higgs field as follows

$$\begin{aligned}
m_e &= \frac{\sqrt{2}}{2}\lambda_1^e\nu \\
m_\mu &= \frac{\sqrt{2}}{2}\lambda_2^\mu\nu \\
m_\tau &= \frac{\sqrt{2}}{2}\lambda_3^\tau\nu
\end{aligned} \qquad (1.33)$$

Quarks :

Following the expression of quarks, the term $\overline{Q}_{iL}\Phi U_{Rj}$ has a non conserved hypercharge, therefore using the propriety of SU(2)[3], we can do the following transformation on Φ like

$$\tilde{\Phi} = i\sigma^2\Phi \quad \Rightarrow \quad \tilde{\Phi} = \frac{\sqrt{2}}{2}\begin{pmatrix} \nu + H \\ 0 \end{pmatrix} \quad , Y(\tilde{\Phi}) = -1 \qquad (1.34)$$

The new expression of the lagrangian becomes :

$$\mathcal{L}_{Yukawa}^{quarks} = -\Lambda_{ij}^{up}\overline{Q}^{iL}\tilde{\Phi}U_{Rj} - \Lambda_{ij}^{down}\overline{Q}^{iL}\Phi D_{Rj} + h.c \qquad (1.35)$$

However, if we chose a basis say the family $\{u, c, t\}$ basis [21] , we can diagonalize one of the matrices like $\Lambda_{ij}^{up} = \lambda^i\delta_{ij}$.so the masses of the up quarks:

$$m_i^{(up)} = \frac{\sqrt{2}}{2}\lambda_i^{(up)}\nu \qquad i = u, c, t \qquad (1.36)$$

The matrice Λ_{ij}^{down} remains non diagonal, in order to set the mass matrix of down quarks fields diagonal, we implement a unitary transformation $\mathcal{V}$ on the basis $\{d, s, b\}$ like:

$$Q'_i = \mathcal{V}_i^j Q_j \Rightarrow \mathbf{m} = \mathcal{V}^\dagger\mathbf{m}\mathcal{V} = diag\{m_d, m_s, m_b\} \qquad (1.37)$$

Where $\mathcal{V}$ is the Cabibbo-Kobayachi-Maskawa(CKM) mixing matrix

---

[3]The fundamental and antifundamental representation of SU(2) are equivalent. therefore,both can be related by unitary transformation

1.2.2 Limites of the Standard Model

After the description of the EW theory , we end up the theory by marrying the EW with the strong Interaction. QCD was a successful QFT to dscribe quarks and gluons interactions, QCD offers a simple explanation of confinement and asymptotic freedom using the renormalization group [26][22], one could show that the coupling constant became smaller at high energies, which could explain the reason why the quarks behaved as if they were free known as asymptotic freedom. similarly at low energies where the coupling constant becomes strong and lead to confinement .

The gauge group that describes the quarks is SU(3) (not like SU(3) of flavor symmetry), where each quark forms a triplet under "color symmetry" like

$$\Psi_C^i = \begin{pmatrix} \Psi_R \\ \Psi_G \\ \Psi_B \end{pmatrix} \qquad i = u, d, c, s, t, b \tag{1.38}$$

And the gauge quanta that mediating the quarks interactions are gluons, denoted as $G_\mu^a, a = 1...8$. the QCD lagrangian that describes the strong interactions is giving by:

$$\mathcal{L}_{QCD} = -\frac{1}{4}\mathcal{G}_{\mu\nu}^a \mathcal{G}_a^{\mu\nu} + i\overline{\Psi}_C^i \not{D}\Psi_{Ci} \tag{1.39}$$

Where the covariant derivative and the strong Tonsor field is giving by

$$\begin{aligned} \mathcal{D}_\mu &= \partial_\mu - ig_s \frac{\lambda_a}{2} G_\mu^a \\ \mathcal{G}_{\mu\nu} &= \lambda_a \mathcal{G}_{\mu\nu}^a = -\frac{2i}{g_s}[D_\mu, D_\nu] \\ &= \partial_\mu G_\nu^a - \partial_\nu G_\mu^a + g_s f^{abc} G_\mu^b G_\nu^c \end{aligned} \tag{1.40}$$

The λ^a are Gellman matrices that satisfies the non-abelian nature of SU(3) and f^{abc} are the structue constants and g_s the coupling constant .

Thus, the Standard Model combines EW theory and QCD in one Master group to describe all fundamental particles and their interactions at subatomic level, which makes it an Effective Field Theory of a Unified Field Theory..

Although the SM has been remarkably successful in accurately describing experimental observations, it is never regarded as a complete theory of physics.The theory cannot explain a lot of ambiguities, either the observed ones nor the ones within the theory, we lists the main limits of the SM that cannot explained :

⋄ The Standard Model is unable to include gravity in a QFT framework, due that gravity is described by a Diffeomorphism Classical Field Theory known as General Relativity [22]. and The Renomalization strategy couldn't suppress the infinities .

⋄ The Heirachy problem between the planck scale and the EW scale , but also the heirachy problem of the Higgs mass, when one try to perform the qunatum corrections in second-loop yukawa coupling, the mass of the Higgs diverges to High Energy Scales (GUT to planck scale)

⋄ The SM has quit a lot of parameters, and cannot explain the origine of neutrinos masses claimed by neutrinos expirements

⋄ The astrophysical observations claims the existens of another type of matter that significanlty large than baryonic matter and has a gravitational effect, doesn't interact with light and matter, it's what so-called Dark Matter. and also the mystery of accelerating expanding universe due to unknown type of energies called Dark Energy

Even though, SM is still the basic framework of the LHC expirements and other expirements, it's was revolutionary acheivement of modern physics from huge contributions of the great physicisits of all time.

1.3 Production of the Higgs boson at LHC

At the LHC, we are interested in producing the Higgs boson[11, 10, 16] in proton-proton collisions and studying its decays. So, we must first understand production mechanisms . At a proton-proton collider, the initial state consist of quarks and gluons . The largest coupling for Higgs production is via the top quark, but the top content of the proton is effectively zero. However, the top Yukawa coupling can be accessed through a gluon- initiated loop or via $t\bar{t}$ pair production (Figure1.3) . By far the largest cross section is for the gluon-initiated top loop (also called gluon-gluon fusion, or ggF)

(a) Vector boson fusion production

(b) production associated with W/Z

(c) gluon fusion production

(d) production associated with tt pairs
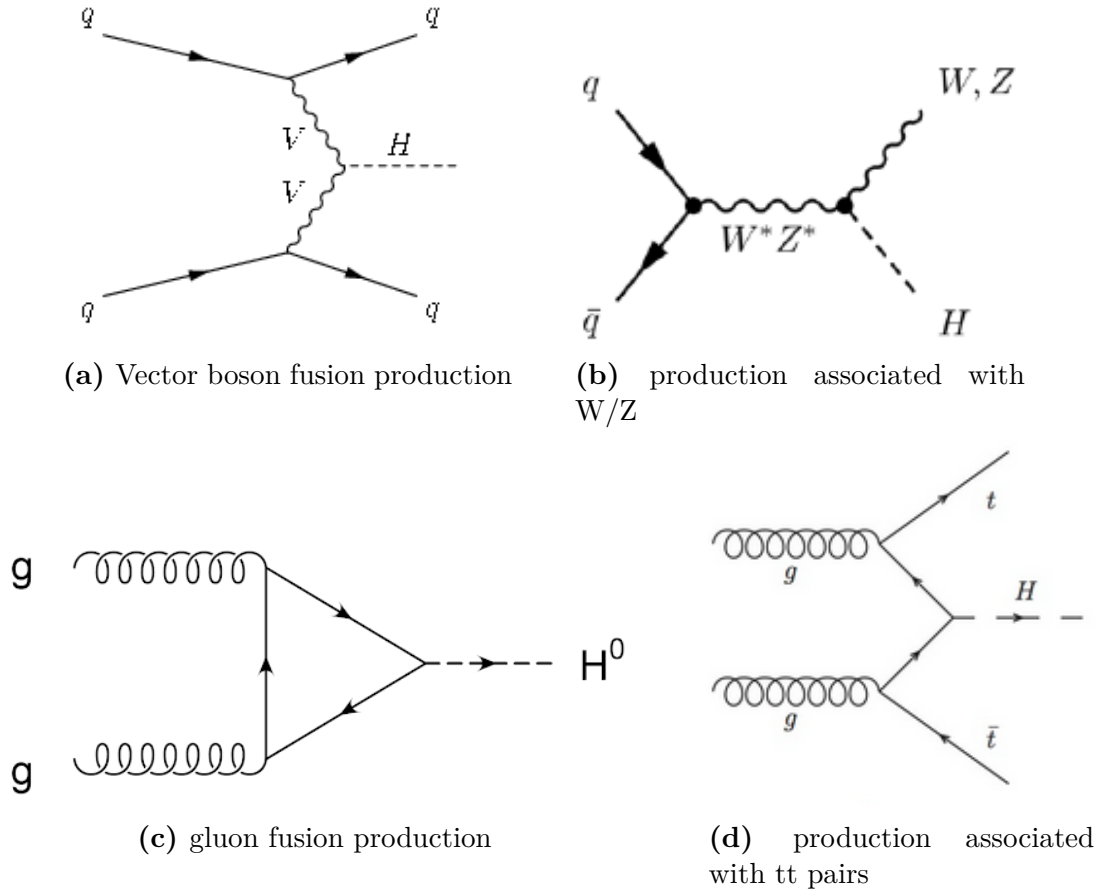
Figure 1.3: Modes of production of Higgs boson at LHC

Alternately, the Higgs can be produced via its couplings with the W and Z bosons. The dominant process here is weak vector boson fusion (VBF), where the Higgs propagator is connected to a t- channel W or Z exchanged between two quarks.Apart from VBF, the Higgs can simply be produced via radiation from an s-channel W or Z boson. This is referred to as "associated production" or "Higgsstrahlung".

Chapter 2

Dark Matter detection at LHC

There are many models that try to provide an explanation for dark matter. One is that DM is made up of axions, which are very light particles associated with a field proposed to solve an entirely different problem (to address the question of why the strong interaction conserves CP symmetry). Collider experiments are generally not sensitive to axions, so they will not be considered further here.

Arguably the most popular DM candidate is the "Weakly Interacting Massive Particle" (WIMP). This is the general term for a new stable (at least on the timescale of the universe) particle which somehow interacts with the SM. This particle is considered to have some new field associated with it, so that it can be described in terms of the same quantum field theory as the SM. This field could be of any type (scalar, spinor, vector, etc.). Assuming all particles were in a high-temperature thermal equilibrium in the early Universe, there must be some mechanism for WIMPs to annihilate into SM particles in order to explain their current abundance.

In this chapter we introduce one the phenomenological models of DM called Higgs portal Models of spin1 Vector candidate case,[4, 12, 20, 19].and outline one of the intresting combination search at LHC known as Higgs Invisible combination, Where several analysises targeting the DM signal are combined in one Statistical Model

2.1 Higgs Portal Models

Particle physics proposes a compelling solution to the puzzle of the missing or dark matter (DM) in the Universe, in terms of a colorless and electrically neutral weakly interacting massive particle (WIMP) that is stable at cosmological times and has a mass in the vicinity of the electroweak scale. Such WIMPs are predicted in many extensions of the Standard Model (SM);for instance. A very interesting class of such models is the one in which the DM states interact only through their couplings with the Higgs sector of the theory, the so–called Higgs–portal DM models [4]

2.1.1 Vector Dark Matter Model

One of simplest DM Effective Field Theory is Vector Dark matter model, where the candidate is spin 1 field coupled to the Higgs sector

$$\Delta\mathcal{L}_V = \frac{1}{2}m_V^2 V_\mu V^\mu + \frac{1}{4}\lambda_V (V_\mu V^\mu)^2 + \frac{\lambda_{HVV}}{4}\Phi^\dagger \Phi V_\mu V^\mu \tag{2.1}$$

Where Φ is the SM Higgs doublet, and V_μ is the DM field,After Symmetry breaking the Higgs scalar field acquires a vaccum expectation value and can be decomposed as

$$\Phi = \frac{1}{2}\begin{pmatrix} 0 \\ H + \nu \end{pmatrix} \quad with \quad \nu = 246 GeV \tag{2.2}$$

inducing the trilinear interaction λ_{HVV} between the physical H state and DM pairs and the DM mass term

$$M_V^2 = m_V^2 + \frac{1}{4}\nu^2 \lambda_{HVV} \tag{2.3}$$

The vector Higgs–portal model formulated above is extremely simple and predictive, featuring only M_V and λ_{HVV} as free parameters. A requirement for the DM particle that is usually made is to lead to the correct cosmological relic density . If the conventional freeze–out paradigm is assumed, it is determined by the thermal average $< \sigma\nu >$ of the DM pair annihilation cross section, which encodes the information from particle physics.

In order to assess the theoretical consistency of the effective Higgs–portal in the vector DM case, in particular for what concerns the interpretation of the searches for invisible Higgs decays, we compare it in the following with one of its simplest and most economical ultraviolet complete realizations: the one in which the vector DM couplings are generated through the mixing of the SM–like Higgs boson with an additional scalar state. We briefly review below the essential features of such a scenario.

$$V(h,s) = \frac{1}{2}\mu_H^2 H^2 + \frac{1}{2}\mu_S^2 S^2 + \frac{\lambda_{HS}}{4}H^2 S^2 + \frac{\lambda_S^2}{4}S^4 + \frac{\lambda_H^2}{4}H^4 \qquad (2.4)$$

After electroweak symmetry breaking, the fields H and S acquire vacuum expectation,values ν and ω which, in terms of the above Lagrangian parameters, can be written as

$$\nu^2 \equiv \frac{2\lambda_{HS}\mu_S^2 - 4\lambda_S\mu_H^2}{4\lambda_H\lambda_S - \lambda_{HS}^2} \qquad , \omega^2 \equiv \frac{2\lambda_{HS}\mu_H^2 - 4\lambda_H\mu_S^2}{4\lambda_H\lambda_S - \lambda_{HS}^2} \qquad (2.5)$$

The Mass matrix can be written

$$\mathcal{M}^2 = \begin{pmatrix} 2\lambda_H\nu^2 & \lambda_{HS}\nu\omega \\ \lambda_{HS}\nu\omega & 2\lambda_S\omega^2 \end{pmatrix} \qquad (2.6)$$

Since the coupling are real, and $\nu^2 > 0 \ \omega^2 > 0$, the Mass matrix is positive definite if and only if

$$\lambda_h > \frac{\lambda_{HS}^2}{4\lambda_S} \quad , \lambda_S > 0 \qquad (2.7)$$

$\mathcal{M}^2$ can be diagonalised by an orthogonal transformation $O^\mathsf{T}\mathcal{M}^2 O = diag(m_{H_1}^2, m_{H_2}^2)$, Where

$$O = \begin{pmatrix} \cos(\theta) & \sin(\theta) \\ -\sin(\theta) & \cos(\theta) \end{pmatrix} \qquad (2.8)$$

and the angle θ satisfies

$$\tan(2\theta) = \frac{\lambda_{HS}\nu\omega}{\lambda_S\omega^2 - \lambda_H\nu^2} \qquad (2.9)$$

The mass eigenvalues are then given by

$$m^2_{H_{1,2}} = \lambda_H \nu^2 + \lambda_S \omega^2 \mp \frac{\lambda_S \omega^2 - \lambda_H \nu^2}{\cos(2\theta)} \qquad (2.10)$$

With H_1 is identified with the Higgs discovered at LHC. and adopting that $[m_{H_2}, \sin(\theta), \lambda_{HS}]$ are free parameters, In terms of the set of free parameters , the couplings of the H1 and H2 states among themselves and with the SM fermions and gauge bosons are given by

$$\mathcal{L}_S^{SM} = (H_1 \cos(\theta) + H_2 \sin(\theta))(2M_W^2 W_\mu^+ W^\mu + M_Z^2 Z_\mu Z^\mu - m_f \bar{f} f)/\nu,$$
$$\mathcal{L}_S^{tril} = -\frac{\nu}{2}(\kappa_{111} H_1^3 + \kappa_{112} H_1^2 H_2 \sin(\theta) + \kappa_{221} H_1 H_2^2 \cos(\theta) + \kappa_{222} H_2^3) \qquad (2.11)$$

adapting $\Delta m_H^2 = m_{H_2}^2 - m_{H_1}^2$, The new couplings canstantes can be written then

$$\kappa_{111} = \frac{m_{H_1}^2}{\nu^2 \cos(\theta)} \Big(\cos^4(\theta) - \sin^2(\theta) \frac{\lambda_{HS} \nu^2}{\Delta m_H^2} \Big)$$

$$\kappa_{112} = \frac{2m_{H_1}^2 + m_{H_2}^2}{\nu^2} \Big(\cos^2(\theta) + \frac{\lambda_{HS} \nu^2}{\Delta m_H^2} \Big)$$

$$\kappa_{221} = \frac{2m_{H_2}^2 + m_{H_1}^2}{\nu^2} \Big(\sin^2(\theta) - \frac{\lambda_{HS} \nu^2}{\Delta m_H^2} \Big) \qquad (2.12)$$

$$\kappa_{222} = \frac{m_{H_2}^2}{\nu^2 \sin(\theta)} \Big(\sin^4(\theta) + \cos^2(\theta) \frac{\lambda_{HS} \nu^2}{\Delta m_H^2} \Big)$$

The vector DM Higgs–portal scenario can be introduced in the setup depicted above by identifying the field S and the vectorial DM candidate V as, respectively, the Higgs and the gauge boson of a new, spontaneously broken, U(1) gauge symmetry.

$$\mathcal{L}_{hidden} = -\frac{1}{4} V_{\mu\nu} V^{\mu\nu} + (D^\mu S)^\dagger (D_\mu S) - V(H, S) \qquad (2.13)$$

Where $V_{\mu\nu} = \partial_\mu V_\nu - \partial_\nu V_\mu$ is the DM field strength and $D_\mu = \partial_\mu + i\tilde{g} V_\mu$ with $\tilde{g}$ being the new gauge coupling. The potential $V(H, S)$ has the same form as the one given in eq 2.4

Upon the spontaneous breaking of the U(1) symmetry, the DM state acquires a mass $M_V = 12\tilde{g}\omega$ and its interactions with the physical state ρ of the original field $S = \frac{1}{\sqrt{2}}(\omega + \rho)$ are given by

$$\mathcal{L}_{DM} = \frac{1}{2}\tilde{g}^2\omega\rho V_\mu V^\mu + \frac{1}{8}\tilde{g}^2\rho^2 V_\mu V^\mu = \frac{1}{2}M_V\rho V_\mu V^\mu + \frac{1}{8}\tilde{g}^2\rho^2 V_\mu V^\mu \qquad (2.14)$$

After electroweak symmetry–breaking and the subsequent mass mixing between h and ρ, the complete interaction Lagrangian, relevant for the DM phenomenology, is then

$$\mathcal{L} = \frac{1}{2}\tilde{g}M_V(H_2 c_\theta - H_1 s_\theta)V_\mu V^\mu + \frac{1}{8}\tilde{g}^2(H_1^2 - 2H_1 H_2 s_\theta c_\theta + H_2^2 c_\theta^2)V_\mu V^\mu$$
$$+ \mathcal{L}_S^{SM} + \mathcal{L}_S^{tril} \qquad (2.15)$$

Where we noted $s_\theta = \sin\theta$ and $c_\theta = \cos\theta$, and $\mathcal{L}_S^{SM}, \mathcal{L}_S$ are given in eq 2.11. The effective vector DM Higgs–portal can be obtained by taking the limits $\sin\theta \ll 1$ and $m_{H_2} \ll m_{H_1}$, provided that the theoretical consistency of this limit is verified. First, the coupling $\tilde{g}$ has to remain perturbative,$\tilde{g}^2/(4\pi) \leq 1$. Second, the perturbative unitarity limit of the cross sections for processes of the type $HiHi \to HjHj$ which translates into the limit $\lambda_i \leq O(4\pi/3)$ has to be accounted for.

In this section, We present briefly the Effective Vector Dark Model , where the SM Higgs act as the portal via it's coupling to Vector DM, And also we compared the EFT model with a UV complet model , where the Vector DM is a gauge field of a spontenously broken U(1) dark sector .

2.2   Dark Matter detection at LHC

Direct searches for dark matter (DM) have been carried out by many different dedicated experiments [23, 13, 2, 3, 18, 1]. At the LHC, both direct and indirect searches for models and candidates of DM are performed. Among them, one plausible scenario is Higgs portal interaction with the Weakly Interacting Massive Particle (WIMP) which could be invisible decay products of the 125 GeV Higgs boson.

In this manuscript, we will focus on the Higgs invisible combination senarios of DM channels, five channels designed for Branching ration $\mathcal{B}_{H \to inv}$ sensetivity, asssuming 100% of SM expectation.

The signatures each analysis addresses is shown in Figure 4.2. Each analysis final state is characterised by large value of E_T^{miss} corresponding to the invisible decay of the Higgs boson and additional physics objects to target a specific Higgs boson production mode.

(a) VBF + E_T^{miss}

(b) Jet + E_T^{miss}

(c) $t\bar{t} + E_T^{miss}$

(d) VBF + $E_T^{miss} + \gamma$

(e) $Z(\to)ll + E_T^{miss}$
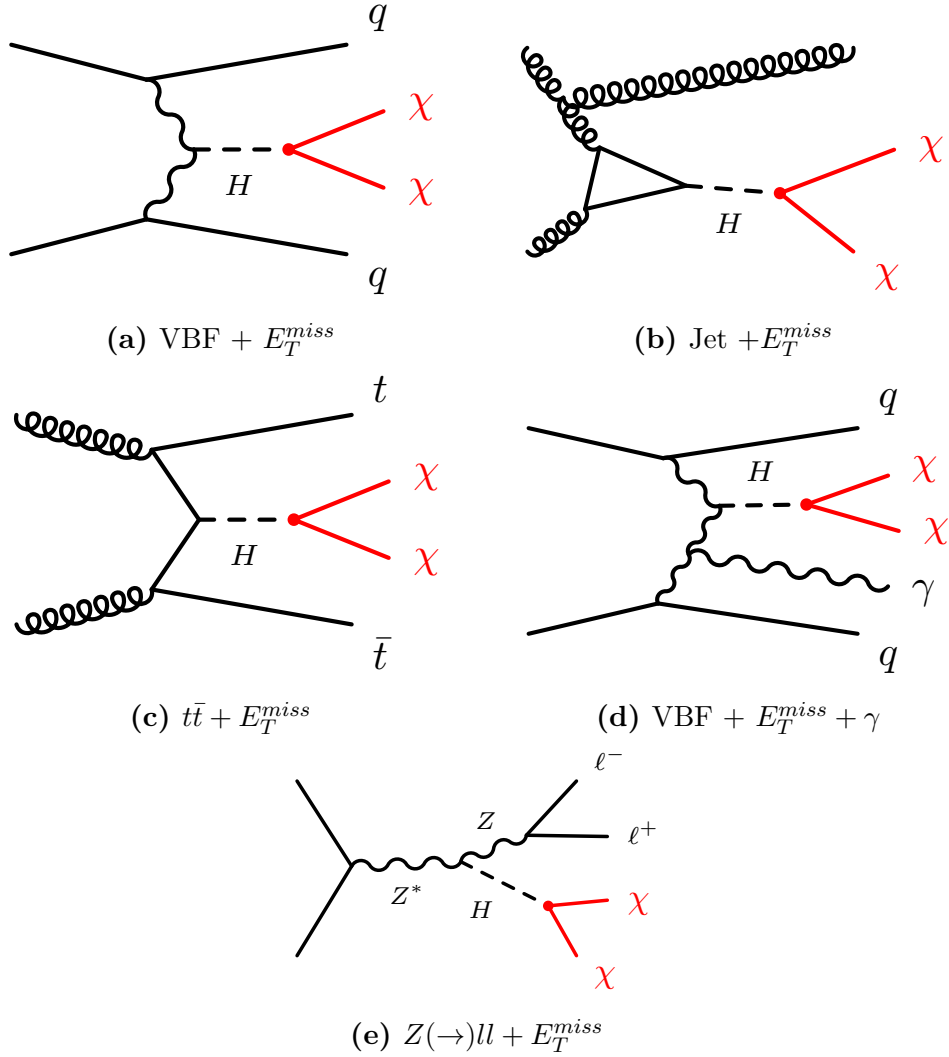
Figure 2.1: Feynman diagrams showing the signals for each input analysis.

2.3 LHC and the ATLAS Detector

2.3.1 LHC

The Large Hadron Collider (LHC) is an accelerator designed to produce proton-proton (pp) and heavy ion (usually Pb-Pb) collisions at the highest energies currently possible. It consists of a 27 km ring of superconducting magnets, as well as several radiofrequency cavities which accelerate the particles.Proton beams

The protons used in the LHC come from an ionized hydrogen source and are first sent through a series of smaller accelerators. These consist of an inital linear accelerator (Linac), Proton Sychrotron Booster, Proton Synchrotron, and Super Proton Synchrotron. After going through all of these steps, the protons each have an energy of 450 GeV, at which point they are injected into the LHC. They are injected in "bunches" of approximately 10^{11} protons, separated by 25 ns.
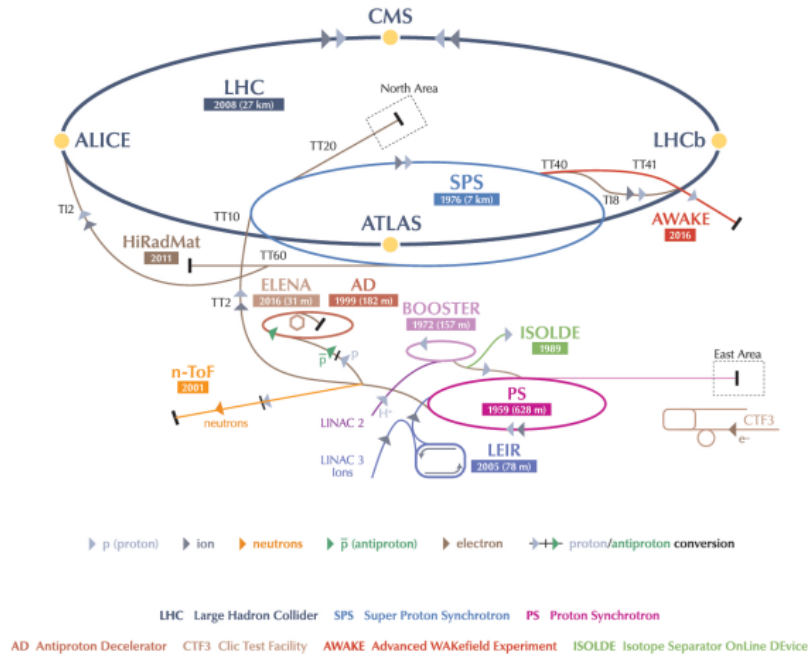
Figure 2.2: Large Hadron Collider accelerator

The two proton beams circulate around the ring in opposite directions and can be focused together (using a set of magnets) to produce collisions at several interaction points. There are four of these interaction points with major detector experiments located at each: ATLAS, CMS, LHCb, and ALICE.

2.4   ATLAS Detector

ATLAS is a general-purpose particle detector located at one of the LHC's interaction points. It consists of several specialized subdetectors which work together to reconstruct leptons, photons,and hadronic jets resulting from the collisions.

The innermost layers form the Inner Detector, which provides tracking for all electrically charge particles. Outside of this are the calorimeters, which measure energy deposits from individual particles or showers. The calorimeters consist of electromagnetic layers (which have fine granularity and are specialized for measuring electrons and photons) and hadronic layers (which capture hadronic showers from jets that penetrate the electromagnetic layers).

The outermost layers of ATLAS form the muon spectrometer, which provides additional tracking specifically for muons, since they generally escape through the entire detector. This section will give a brief overview of each of these main components.

The coordinate system used by ATLAS is a right-handed one with the origin at the nominal interaction point. The z-axis is along the beam pipe, the x-axis points toward the center of the LHC ring, and the y-axis is vertically up. For practical purposes, cylindrical coordinates (r, φ) are generally used in the plane transverse to the z-axis. Here, φ is the azimuthal angle around the z-axis. Another useful coordinate is the pseudorapidity η, which is defined in terms of the polar angle θ as:

$$\eta = -\ln(\tan(\frac{\theta}{2})) \qquad (2.16)$$

This variable is used rather than θ because the difference in η between two objects is invariant under Lorentz boosts along the z-axis. This can all be put together to define a distance measure ΔR between any two objects in (η, φ) and invariant under those same boosts:

$$\Delta R = \sqrt{\Delta\eta^2 + \Delta\varphi^2} \qquad (2.17)$$

where $\Delta\eta$ and $\Delta\varphi$ are the distances between the two objects in η and φ.
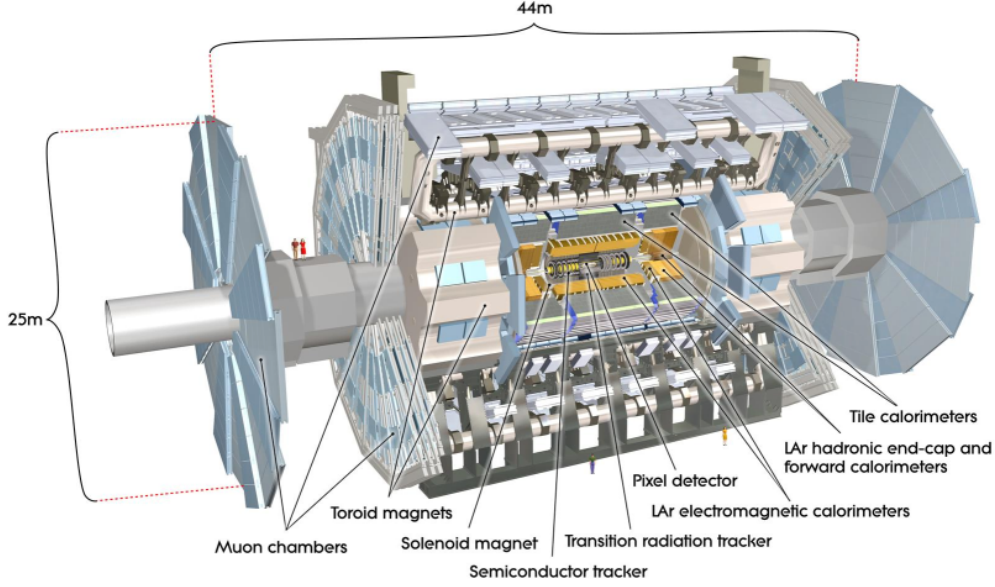
Figure 2.3: ATLAS DETECTOR of CERN

2.4.1 The Inner Detector

The Inner Detector serves the primary purpose of measuring the trajectories of charged particles produced in the collisions at ATLAS. It provides this tracking capability in a pseudorapidity range of $|\eta| < 2.5$. It consists of three subdetectors:

The Pixel Detector, the Semiconductor Tracker (SCT), and the Transition Radiation Tracker (TRT). Together, these read out the spatial positions of "hits", where charged particles leave localized energy deposits. These hits are later reconstructed into tracks, which represent that actual path of the particle.

The Pixel detector consists of four cylindrical barrel layers and three disk-shaped endcap layers. Together, these provide tracking information at the smallest radii for $|\eta| < 2.5$. Each layer consists of many sensors.Ionization in the silicon due to charged particles passing through it provides the signal.

The Semiconductor Tracker uses the same basic technology as the Pixels, but the fundamental unit of silicon is a larger "strip". The SCT has four cylindrical barrel layers and nine disk-shaped end-cap layers. This also provides tracking coverage out to $|\eta| = 2.5$.

The Transition Radiation Tracker is the outermost component of the ID, and covers only the region $|\eta| < 2.0$. It uses proportional drift tubes (known as "straws") filled with a gas mixture (usually xenon-based) as the basic detector
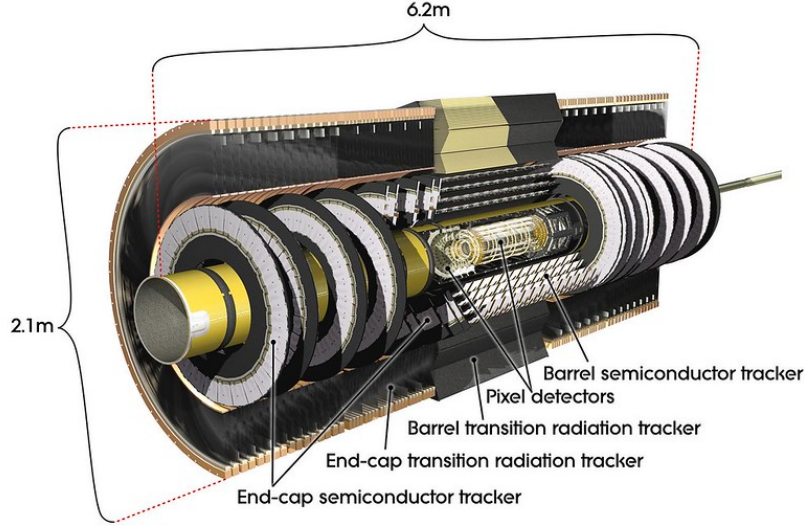
Figure 2.4: General cut-away view of the Inner Detector

element . Each straw consists of a cylindrical cathode, with an anode wire running along its axis. The straw layers are interleaved with polypropylene fibers (in the barrel) or foils (in the end-cap). Since this has a different dielectric constant from the other surrounding materials, charges particles crossing those boundaries emit low-energy (keV-scale) photons, known as transition radiation. These photons ionize the gas in the tubes, which creates an electron avalanche due to the high electric field. The resulting electrons are collected on the anode wire to give a readout signal.

2.4.2   Calorimeters

ATLAS includes two types of calorimeter system for measuring electromagnetic and hadronic showers. These are the Liquid Argon (LAr) calorimeters and the Tile calorimeters. Together, these cover the region with $|\eta| < 4.9$

The Liquid Argon system consists of four individual calorimeters: the Electromagnetic Barrel (EMB), Electromagnetic End-cap (EMEC), Hadronic End-cap (HEC), and Forward Calorimeter (FCAL). These are all sampling calorimeters, which use liquid argon as the active material inter leaved with metal absorber layers. The active regions are equipped with electrodes, which measure the ionization of the argon due to passing particles. The EMB and EMEC are primarily designed around reconstructing electrons and photons, while the HEC and FCal are geared toward measuring hadronic showers (jets).
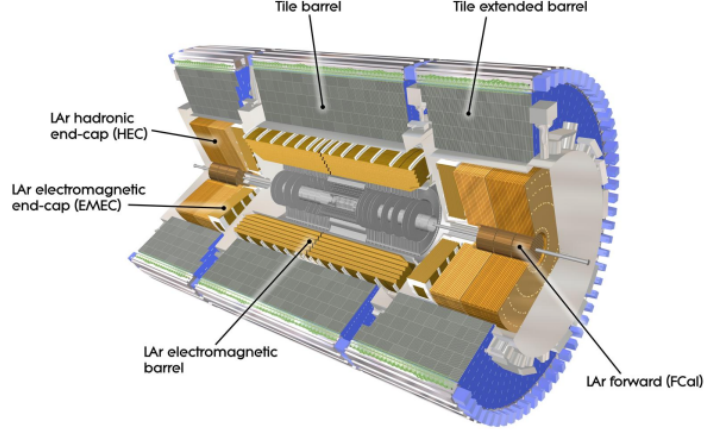
Figure 2.5: General cut-away view of the calorimeters

2.4.3 The Muon Spectrometer

The Muon Spectrometer is the outermost component of the ATLAS detector, and provides tracking for muon reconstruction in the region $|\eta| < 2.7$. Most of the system lies in a large magnetic field provided by a set of toroid magnets. This serves to bend the trajectory of the muons, allowing the reconstruction of their momentum. The MS itself consists of four types of chambers, arranged in a barrel ($|\eta| < 1.05$) and two end-cap sections ($1.0 < |\eta| < 2.7$)
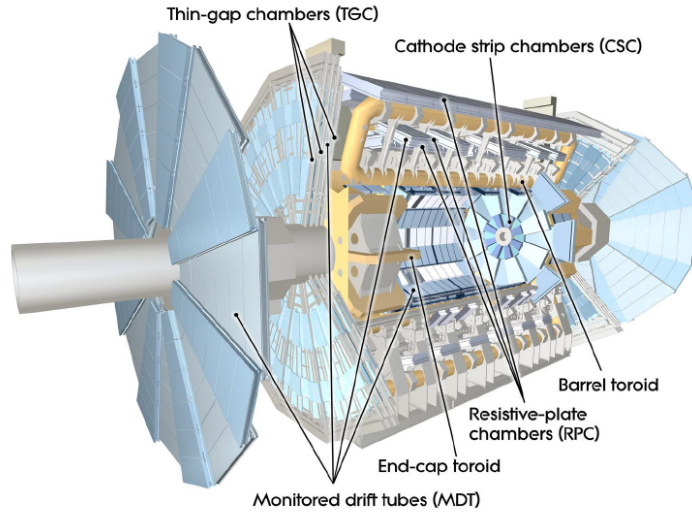
Figure 2.6: General cut-away view of muon sperctrometer

The entire η range is covered by Monitored Drift Tube (MDT) chambers. These provide the best resolution for muon tracking. Each MDT consists of an aluminum tube filled with an argon-based gas mixture and an anode wire running along its axis. When a muon passes through, some of the gas is ionized, and the electrons are collected on the wire to generate a readout signal.

Part II

Experimental Framework

Chapter 3

Overview of Vector Boson Fusion Analysis for Invisible Higgs decays Search

In this chapter we shall foucus on experimental aspect of vector boson fusion for drak matter search, we start with the events selection and signal definition used in VBF search, and also the Control Regions of differents backgrounds and its estimations. and we end the chapter with the interpretation of the DM model as the exclausion limit in branching ration of the nuclous-WIPMs cross section and WIMPs mass phase space , and compare it with direct detection expiremets

We present a search for the decays of the 125 GeV Higgs boson , produced via the vector boson fusion (VBF) process , into invisible particles $(\chi\overline{\chi})$. The hypothesis under consideration is that the Higgs boson might decay into a pair of Weakly Interacting Massive Particles (WIMP)

3.1 Data and MC samples

The analysis is performed using ATLAS data collected in 2015–2018, when the LHC delivered proton– proton collisions at $\sqrt{s} = 13$ TeV. The total integrated luminosity recorded is 147 fb^{-1}. Only events recorded during stable beam conditions and with all ATLAS sub-systems fully operational are considered.The Good Runs Lists (GRL) used are, for a total integrated luminosity of 138.9 fb^{-1} .

.

3.1.1 Signal MC samples

This analysis targets VBF Higgs boson production. The small contributions from the ggF and V H Higgs boson production processes passing the analysis selection are also treated as signal.the sample is generated at a Higgs mass 125 GeV, and the invisible decay of the Higgs is simulated by forcing it to decay into two Z bosons decaying into neutrinos. The difference between this and decays to a new invisible particle is negligible,The SM branching ratio for the invisible Higgs decay is approximately $1, 2.10^{-3}$, however this value floats in the final fit to allow for enhancement by non-SM particles. This table 3.1 summerize the MC generators of the signal modelling

Process	Generator	ME Order	PDF	Parton Shower	Tune
ggF Higgs	POWHEG NNLOPS	NNLO	PDF4LHC15 NNLO	PYTHIA8	AZNLO
VBF Higgs	POWHEG	NLO	PDF4LHC15	PYTHIA8	AZNLO
VH Higgs	PowhegBox v2	NLO	PDF4LHC15	PYTHIA8	ANZLO

Table 3.1: Generators of Signal simulation [8]

3.1.2 Standard Model Background samples

The dominant backgrounds to this analysis arise from single weak boson production in association with jets, denoted V+jets, where the boson decays via $Z \rightarrow \nu\nu$ or $W \rightarrow l\nu$. The $Z \rightarrow ll$ decay modes ($l = e$ or μ) are also important to constrain the $Z \rightarrow \nu\nu$ contribution . The V/VV+jets processes are split into two components based on the order in the electroweak coupling constant α_{ewk}

The production of $t\bar{t}$, the associated production of top-quarks with W bosons (tW), and single-top s-channel and t-channel production are modelled using the powhegbox generator at NLO with the NNPDFNLO PDF set.QCD multijet production is generated using pythia8.230 with leading-order matrix elements for dijet production interfaced to a p_T ordered parton shower.The Table 3.2 summerize the MC generators of background modelling

Process	Generator	ME Order	PDF	Parton Shower	Tune
Strong V+jets	SHERPA v2.2.1, SHERPA v2.2.7 (m_{jj}-filtered)	NLO (up to 2-jets), newline LO (up to 4-jets)	NNPDF3.0nlo	SHERPA MEP-SATNLO	SHERPA
Electroweak V+jets	SHERPA v2.2.1 reweighted byHERWIG7 in m_{jj}	LO (up to 4-jets), NLO (reweighting)	NNPDF3.0nlo	SHERPA MEPSATLO	SHERPA
VV+jets (including $gg \to VV$+jets)	SHERPA v2.2.1 orSHERPA v2.2.2	NLO (up to 1-jet), LO (up to 3-jets)	NNPDF3.0nl	SHERPA MEP-SATNLO	SHERPA
Electroweak VV+jets	SHERPA v2.2.1 orSHERPA v2.2.2	LO	NNPDF3.0nlo	SHERPA MEPSNLO	SHERPA
V+jets α_{ewk}^3 interference	MGMCatNLO	LO	PDF4LHC15	PYTHIA8	
$t\bar{t}$	POWHEGBOX v2	NLO	NNPDF3.0nlo	PYTHIA8	A14
QCD multijet	PYTHIA 8.230	LO	NNPDF2.3nlo	PYTHIA8	A14

Table 3.2: Summary of generators used for simulation. [8]

3.2 Object definition and Recontruction

In pp collision inside ATLAS, differents particles and jets penetrates into the detector and they leave energy deposits turns into data or what so-called raw data, this raw data can transformed into objects or what so-called recontruction algorithms. we have three types of particles that can be recontructed, leptons and jets and photons.and also the missing transvers energy (MET)

3.2.1 Electrons

Electrons are reconstructed from insertable a combination b-layer of calorimeter and Inner Detector information. A typical electron traverses the entire Inner Detector, leaving a track in the form of hits in the individual layers. In the TRT, many of these are "high-threshold" hits , which distinguishes electrons from heavier charged particles.Then, the electron deposits its remaining energy entirely in the EM layers of the calorimeter.

Once the electron candidate has been established, it is passed through an identification algorithm in order to remove backgrounds.The algorithm itself uses a likelihood-based discriminant constructed from the full set of input variables. Several working points for the identification ("Loose", "Medium", and "Tight") are defined by choosing different values of the discriminant to cut on.

To be considered in the analysis, electrons are required to have $p_T > 4.5$ GeV and to be within $|\eta| < 2.47$ (including the crack region). The electrons may be within the transition regions between barrel and endcap EM calorimeters at $1.37 < |\eta| < 1.52$. Several working points for the identification ("Loose", "Medium", and "Tight") are defined by choosing different values of the discriminant to cut on.The selection criteria for different signal events and veto are collected in Table 3.3

Electron selection			
Feature	*Veto*	*W Signal*	*Z Signal*
Pseudorapidity range	$|\eta| < 2.47$ (including the crack region)		
Energy calibration	"es2018_R21_v0" (ESModel)		
Transverse energy	$E_T > 4.5$ GeV	$E_T > 30$ GeV	$E_T > 4.5$ GeV
Object quality	Not from a bad calorimeter cluster (BADCLUSELECTRON) Remove clusters from regions with EMEC bad HV (2016 data only)		
Track to vertex association	-	$|d_0^{\mathrm{BL}}(\sigma)| < 5$ $|\Delta z_0^{\mathrm{BL}} \sin\theta| < 0.5$ mm	
Identification	LooseBLayer	TightLH	LooseBLayer
Isolation	-	FixedCutLoose (FixedCutHighPtCaloOnly for $p_T > 200$ *GeV*)	

Table 3.3: Summary of electron selections [8].

3.2.2 Muons

Due to lepton universality, muons are always produced exactly the same as electrons at the LHC (up to the mass difference). However, due to their larger mass, muon leave a very different signature in the detector. Where electrons deposit all of their energy in the calorimeters, muons traverse the entire detector and escape.

Tracks from both the Inner Detector and the Muon Spectrometer are used in muon reconstruction. The ID tracks are exactly the same as those used in electron reconstruction . MS tracks are built by first constructing "segments" from hits in the individual muon subdetectors. A combinatorial fit is then run on these segments to get full track candidates.

To be considered in the analysis, muons are required to have $p_T > 4$ GeV and to be within $|\eta| < 2.7$. They must also pass a set of "VeryLoose" track quality criteria. The Muon selection is summerized in Table 3.4

Muon selection			
Feature	*Veto*	*W Signal*	*Z Signal*
Selection Working Point	Very Loose	Medium	Loose
Isolation Working Point	-	FCLoose	
Momentum Calibration	Sagitta Correction is used		
p_T Cut	4 GeV	30 GeV	4 GeV
$|\eta|$ Cut	2.7	2.5	2.7
Overlap removal	no	yes	yes
Track to vertex association	-	$|d_0^{\mathrm{BL}}(\sigma)| < 3$ $|\Delta z_0^{\mathrm{BL}} \sin\theta| < 0.5$ mm	

Table 3.4: Summary of muon selections [8].

3.2.3 Photons

Photon candidates are reconstructed from clustered energy deposits in the electromagnetic calorimeter . Photons and electrons are overlap distinguished using the ambiguity resolver. To be considered in the analysis, photons are required to have $p_T > 20$ GeV and to be within $|\eta| < 2.37$. The photons may not be within the transition regions between barrel and endcap EM calorimeters at $1.37 < |\eta| < 1.52$. They must also satisfy object quality requirements encoded in the EGamma BADCLUSELECTRON bitmask. Photons must pass "Loose" likelihood based identification for overlap removal. The identification requirement is "Tight" likelihood based identification criteria and pass the "FixedCut-Tight" isolation criteria for photon counting (e.g. "Signal" photons). Selections are summarized in Table 3.5

Baseline Photon selection	
Feature	*Criteria*
Pseudorapidity range	$\lvert\eta\rvert < 2.37$
Energy calibration	"$es2018_R21_v0$" (ESModel)
Transverse energy	$E_T > 20$ GeV
Object quality	Not from a bad calorimeter cluster (BADCLUSPHOTON)
	Remove clusters from regions with EMEC bad HV (2016 data only)
Photon cleaning	passOQquality
Fudging	Applied for Full sim / not for AtlFastII
Identification	Loose
Signal Photon selection	
Identification	Tight
Isolation	FixedCutTight

Table 3.5: Summary of photon selections [8].

3.2.4 Jets

Jets (showers of hadrons originating from a quark or gluon) are reconstructed from energy deposits in the hardronic calorimeter. For each event, the energy of each calorimeter cell is read out and the cells are then grouped into topological clusters.

The particle flow (PFlow) algorithm suppresses calorimeter energy deposits arising from charged pileup particles and takes the momentum estimation from tracks whenever the tracker resolution is better than the calorimeter resolution. PFlow jets are constructed with the anti-k_t algorithm[14] with a size parameter value of R = 0.4 using charged constituents associated with the primary vertex and neutral PFlow constituents as inputs.

To be considered in the analysis, jets are required to have $p_T > 25$ GeV, with $\lvert\eta\rvert < 4.5$. The Jet Vertex Tagger (JVT) discriminant is used to identify jets originating from the hard-scatter interaction through the use of tracking and vertexing information. Jets with $p_T < 60$ GeV and $\lvert\eta\rvert < 2.4$ are required to satisfy the requirement JVT > 0.20, corresponding to a selection efficiency for hard-scatter jets of about 98% .This is the "Medium" JVT working point for PFlow jets.

Furthermore, the leading two jets (of this analysis) must pass a threshold on the forward jet vertex tagger (fJVT)] of less than 0.5 or 0.2 for the "Loose" and "Very Tight" operating points, respectively. The "Very Tight" operating point was developed for this analysis to reject multijet for events with $E_T^{miss} <$ 180 GeV.the jets selection is summerized in Table 3.6

Jet reconstruction parameters	
Parameter	Value
algorithm	anti-k$_T$
R-parameter	0.4
input constituent	PFlow
Analysis Release Number	21.2.114
CalibArea tag	00-04-82
Calibration configuration	$JES\_MC16Recommendation\_Consolidated\_PFlow\_Apr2019\_Rel21.config$
Calibration sequence (Data)	$JetArea\_Residual\_EtaJES\_GSC\_Insitu$
Calibration sequence (MC)	$JetArea\_Residual\_EtaJES\_GSC$
Selection requirements	
Observable	Requirement
Jet cleaning	LooseBad
BatMan cleaning	No
p_T	>25 GeV
$|\eta|$	<4.5
JVT	>0.50 for p_T <60 GeV , $|\eta| < 2.5$
fJVT	Leading two jets (< 0.5 Loose for $E_T^{miss} > 180\ GeV$)
	Leading two jets (< 0.2 Very Tight for $E_T^{miss} \leq 180\ GeV$)

Table 3.6: Summary of jet selections [8].

3.2.5   Missing Energy Transvers MET

Not all particles can be directly reconstructed with ATLAS. Neutrinos, as well as any dark matter candidate, do not interact with the detector via electromagnetic or strong interactions. So, their presence can only be inferred from an imbalance of transverse momentum in the event (denoted E^{miss}, sometimes also abbreviated as "MET"). As this is a search for the production of invisible particles, the reconstruction of this object is crucially important.

At the simplest level, the E_T^{miss} in a given event is defined as the negative vector sum of all reconstructed objects in the event(electrons,jets,muons).However, there is often additional soft activity in the event (such as objects below the reconstruction threshold or soft radiation). For this reason, a "soft term" is also included in the E_T^{miss} definition. The soft term can be calculated either from calorimeter information (the Cluster Soft Term, CST) or from ID tracks (the Track Soft Term, TST). The full definition is then

$$\overrightarrow{E_T}^{miss} = - \sum_{jets} \overrightarrow{p_T}^{jets} - \sum_{elec} \overrightarrow{p_T}^{elec} - \sum_{muons} \overrightarrow{p_T}^{muons} - \sum_{tracks} \overrightarrow{p_T}^{tracks} \qquad (3.1)$$

In the control samples with one or more signal leptons, the E_T^{miss} is adjusted such that those leptons are treated as invisible particles.for the one electron control regions, an E_T^{miss} significance variable is used to enrich the contribution from multijet events with a fake electron:

$$S_{\mathrm{MET}} = \frac{E_T^{miss}}{\sqrt{p_T^{j1} + p_T^{j2} + p_T^{e}}}, \qquad (3.2)$$

where the upper indices specify the two highest p_T jets (j1 and j2) as well as

the electron (e). To suppress the background from multijet events for which the E_T^{miss} is stemming from unidentified pile-up jets, or jets being mis-tagged as pile-up, the variable H_T^{miss} [8] is defined as the magnitude of the vectorial sum of the transverse momenta of *all* jets with $p_T > 20\,GeV$, including pile-up jets.

3.3   Overlap Removal

In some cases, ambiguities can arise when multiple objects are identified at the same location in (η, φ). For example, high-p_T electrons are nearly always identified as jets, and jets from b-hadron decays often contain muons which pass the muon identification. In order to avoid double-counting, an overlap removal procedure is applied.

The photons overlap with the electrons, muons and jets uses the default ΔR overlap removal, where ΔR is calculated using rapidity by default.A summary of the overlap removal is given in Table 3.7

Reject	Against	Criteria
electron	electron	shared track, $p_{T,1} < p_{T,2}$
muon	electron	is calo-muon and shared ID track
electron	muon	shared ID track
photon	electron	$\Delta R < 0.4$
photon	muon	$\Delta R < 0.4$
jet	electron	$\Delta R < 0.2$
electron	jet	$\Delta R < \min(0.4, 0.04 + 10\,GeV/p_T^{\mathrm{e}})$
jet	muon	NumTrack < 3 and (ghost-associated or $\Delta R < 0.2$)
muon	jet	$\Delta R < \min(0.4, 0.04 + 10\,GeV/p_T^{\mu})$
photon	jet	$\Delta R < 0.4$

Table 3.7: Overlap removal matching criteria.

.

3.4   Events Selection

3.4.1   Trigger

The data used in this analysis were recorded with an E_T^{miss} trigger. The trigger consists of two levels of selections, the first in hardware, L1, and the second in software, HLT. The L1 trigger use as inputs coarse-spatial-granularity analog sums of the measured energy. The HLT uses EM scale calibrated clusters of cell energies in the calorimeter that are then used to cluster jets.showed in Table 3.8

Period	Trigger
All 2015	HLT_xe70_mht
2016, Runs $\leq$ 302872	HLT_xe90_mht_L1XE50
2016, Runs $>$ 302872	HLT_xe110_mht_L1XE50
2015–2016	HLT_noalg_J400
2017 Runs	HLT_xe110_pufit_L1XE55
2018 Runs	HLT_xe110_xe70_L1XE50

Table 3.8: Triggers used for 2015-2018 data taking [8]

3.4.2 VBF Topology

In VBF topology, the $H \to inv$ signal is characterised by two jets with a wide separation in pseudorapidity and missing energy from the invisible Higgs decay. this two leading jets are more forward than jets from non-VBF processes,This leads to large values of the pseudo-rapidity separation $\Delta\eta_{jj}$ and the invariant dijet mass m_{jj} . In QCD multijet events, the leading two jets exhibit a back-to-back topology $(\Delta\varphi_{jj} \sim \pi)$ in the transverse plane.

(a) vbf

(b) vbf topology
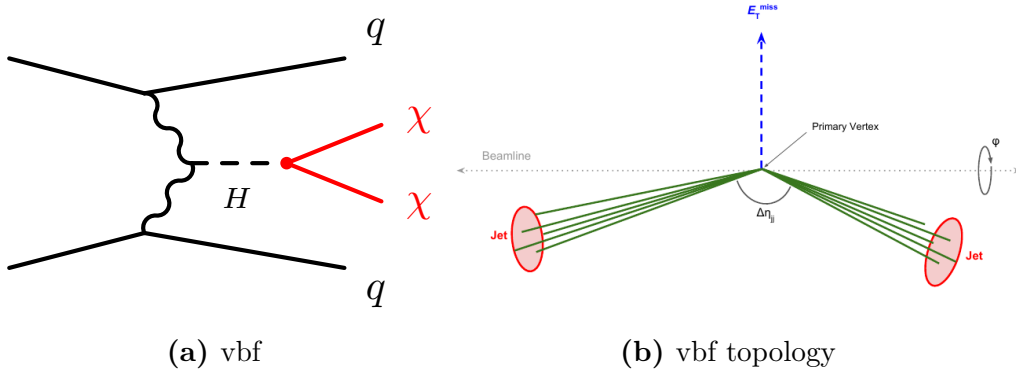
Figure 3.1: Feynman diagramm of VBF precess and typical event signal

Another distinct feature of the VBF process is the large rapidity gap with reduced hadronic activity between the two leading jets, caused by the absence of colour connection between the two quarks. Therefore, to suppress the strong V+jet production with additional jets from QCD radiation, it is required for the largest part of the signal selection that no further jet with $p_T > 25$ GeV is present.However, intial and final state radiation in VBF processes can result in additional jets with $p_T > 25$ GeV. Therefore, to enhance the sensitivity of the analysis, events with three or four jets are considered as well but with additional requirements. The centrality C_i of a third and fourth highest p_T jet ($i = j_3$ and $i = j_4$) is defined as

$$C_i = \exp\left(-\frac{4}{(\eta^{j1} - \eta^{j2})^2}\left(\eta^i - \frac{\eta^{j1} + \eta^{j2}}{2}\right)^2\right). \tag{3.3}$$

Small values of C_i indicate that the additional jet has an η far away from the average value from the two leading p_T jets . To further identify if an extra jet originates from final state radiation of one of the leading two jets, the invariant mass of the extra jet with each of the two leading jets relative to m_{jj} can be used:

$$m_i^{\text{rel}} = \frac{\min\{m_{\text{j1},i}, m_{\text{j2},i}\}}{m_{jj}}. \tag{3.4}$$

Small values of m_i^{rel} indicate that the additional jet is compatible with final state radiation.

3.4.3 Events Selection

Events entering the signal region (SR) must satisfy the following requirements:

- The event contains no lepton candidate, nor a photon.

- The event contains two, three or four jets with $p_T > 25\,GeV$.

- In the case of a third ($i = $ j3) or fourth ($i = $ j4) jet, the centrality of the additional jets must fulfil $C_i < 0.6$; for each of those jets m_i^{rel} has to be small: $m_i^{\text{rel}} < 0.05$.

- The event has $E_T^{miss} > 200\,GeV$, which strongly suppresses the multijet background.

- Further suppression of the multijet background is achieved by requiring $H_T^{miss} > 180\,GeV$.

- The leading two jets are not back-to-back: $\Delta\varphi_{jj} < 2.0$.

- The leading two jets lie in opposite longitudinal hemispheres: $\eta^{\text{j1}} \cdot \eta^{\text{j2}} < 0$ and are well separated in η: $\Delta\eta_{jj} > 3.8$.

- The invariant mass of the leading two jets is large: $m_{jj} > 0.8\,TeV$.

The selected events in the SR are split into eleven bins of different signal purity. Events with exactly two jets are separated into five m_{jj} bins (0.8–1.0 TeV, 1.0–1.5 TeV, 1.5–2.0 TeV, 2.0–3.5 TeV, $> 3.5\,TeV$) and are further split into two bins of $\Delta\varphi_{jj} < 1.0$ and $1.0 \leq \Delta\varphi_{jj} < 2.0$. This yields ten SR bins for two-jet events. The highest signal to background ratio is obtained for the largest values of m_{jj}, while the smaller range in $\Delta\varphi_{jj}$ also show a better background suppression. All events with three or four jets form the eleventh bin, which has by construction a lower signal to background ratio. A schematic view of the binning strategy is shown in Fig. 3.2.
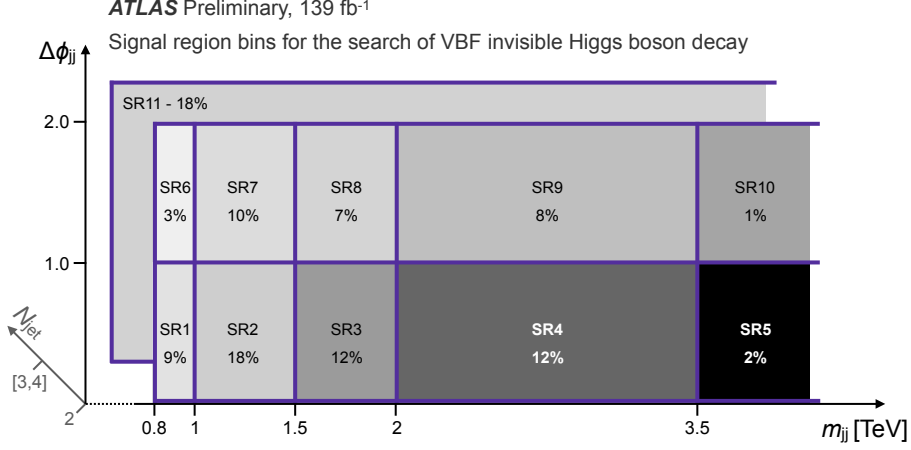
Figure 3.2: Schematic view of the eleven bins in the signal region. The shading indicates the signal to background ratio and a darker grey corresponds to a higher value. The percentage gives the distribution of signal from invisibly decaying Higgs bosons to each of the bins [8].

3.5 Background Estimation

Events from V+jets processes comprise about 95% of the background that enter the SR. Minor backgrounds arise from diboson and $t\bar{t}$ production, which are taken directly from simulation, and from multijet (MJ) processes which are estimated from data.

3.5.1 V + jets background

The background in the SR from V+jets processes are challenging to model, and hence have large associated theoretical uncertainties. To improve the estimation of these backgrounds, a data driven technique known as Transfer-Factor method is implemented that uses control regions (CRs) with selected $Z(\to ll)$+jets and $W(\to l\nu)$+jets events. Each CR is divided into eleven bins corresponding to the SR bin definition (described in Sec. 3.4.3)

The $Z(\to ll)$ CR is based on the same selection criteria as the SR, but the lepton veto is replaced by the requirement of exactly two same-flavour opposite-sign "signal" leptons l with $|m_{ll} - m_Z| < 25\,GeV$. The leading lepton-p_T threshold is $30\,GeV$ while for the sub-leading lepton no further requirement on p_T is made.

To suppress contamination from VV and VVV production, as well as contributions from VBF $H \to W^*W$ or $H \to \tau^+\tau^-$ the event is required to have $E_T^{miss} < 70\,GeV$, This exploits the fact that events from those processes are expected to have larger amounts of E_T^{miss}. A comparison of the observed yield in the Z_{ll} CR and the expectation from simulation is shown in Fig. 3.3.
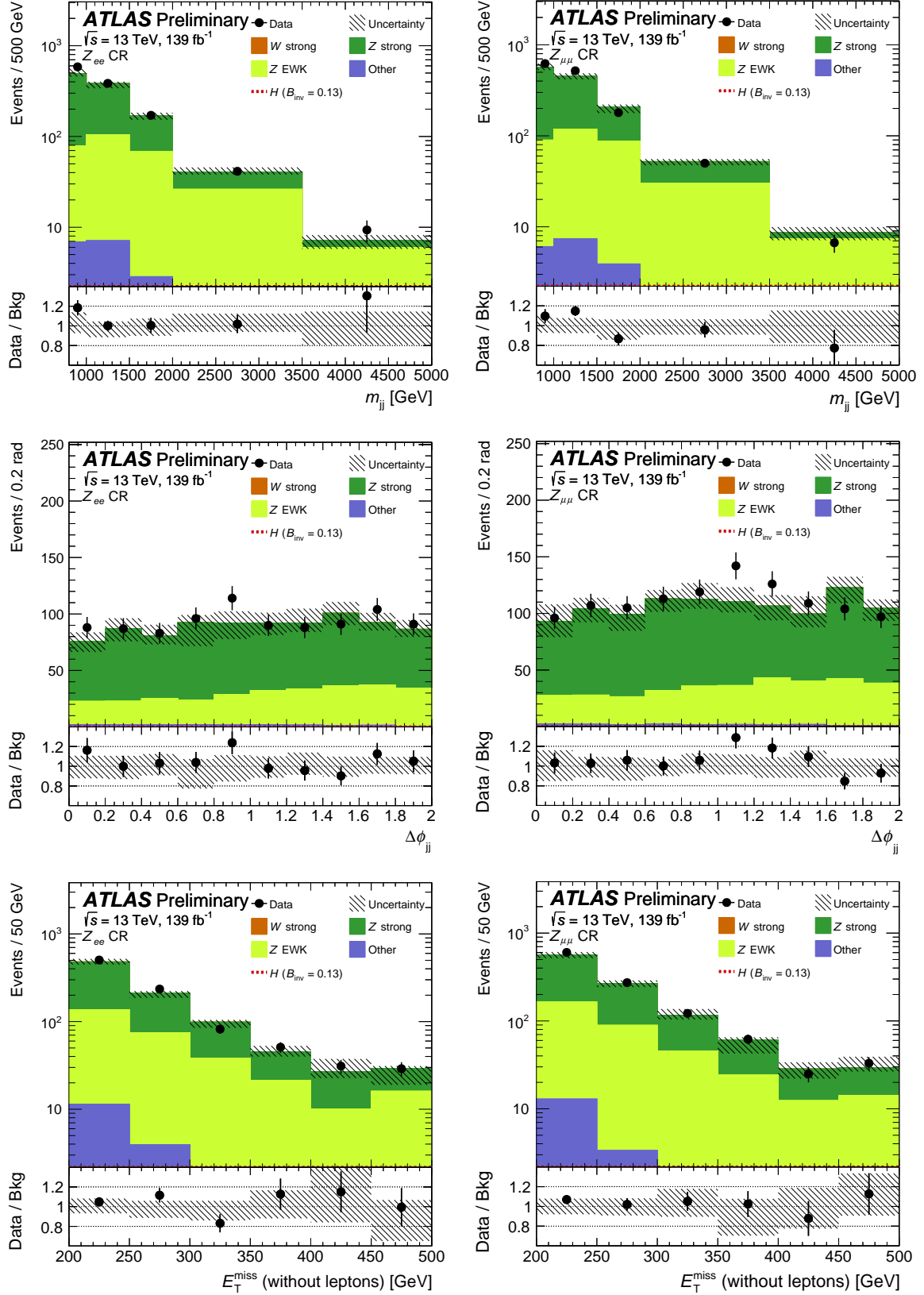
Figure 3.3: Distributions of m_{jj}, $\Delta\varphi_{jj}$, and E_T^{miss} (without leptons) in the Z_{ll} control region for Z_{ee} (left) and $Z_{\mu\mu}$ (right).. Minor contributions from $t\bar{t}$, VV, VVV, and VBF H with $H \to \tau^+\tau^-$ or $H \to W^*W$ are summed up as "Other". The hatched band indicates statistical and reconstruction systematic uncertainties. [8]

3.5.2 Fake electrons in W$e\nu$ CR

The W CRs require exactly one "signal" lepton with $p_T > 30\,GeV$. The remaining selection criteria are identical to those of the signal region. Events that pass this selection are divided by the lepton flavour, and for the single-muon control region ($W_{\mu\nu}$ CR) no further selection is applied. The single-electron sample is expected to have a contribution of events with fake electrons originating from multijet processes in which a jet is mis-identified as an isolated electron. To suppress this contribution, the events in the single electron control region ($W_{e\nu}$ CR) are further required to pass $S_{\mathrm{MET}} > 4[GeV]^{\frac{1}{2}}$. The single-electron events that fail this S_{MET} selection define the "fake-e CR", which is enriched by fake electrons. To evaluate the fake-electron background in the $W_{e\nu}$ CR, another control region ($W_{e\nu}$ anti-ID) enriched with fake electrons is defined with the electron passing a loose identification requirement but not the tight one of "signal" leptons (see Fig. 3.4, left).
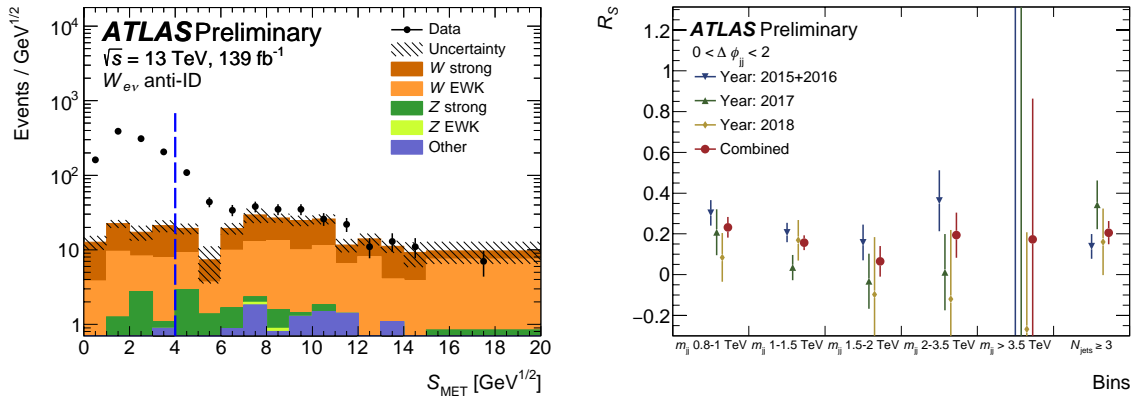
Figure 3.4: The left figure shows a comparison of the S_{MET} distribution in data and simulation for the $W_{e\nu}$ anti-ID control region, for which the electron passes a loose identification but not the tight one. The right figure shows the ratio R_S of number of events with high S_{MET} to those with low values as a function of m_{jj} for three years of data-taking (2016, 2017, and 2018) separately. [8]

For this selection the ratio R_S of the number of data events with high S_{MET} to the number with low S_{MET} is calculated after the W, Z, VV, and $t\bar{t}$ backgrounds are subtracted. To reduce the statistical uncertainties, the ratio R_S is averaged over the years, but is binned in m_{jj} (see Fig. 3.4, right).

The ratio R_S is then used to scale the fake-electron contribution in the "fake-e" CR to obtain the expected background of fake electrons in the $W_{e\nu}$ CR at high S_{MET}. A comparison of the observed yield in the W CRs and the expectation from simulation is shown in Fig. 3.5.
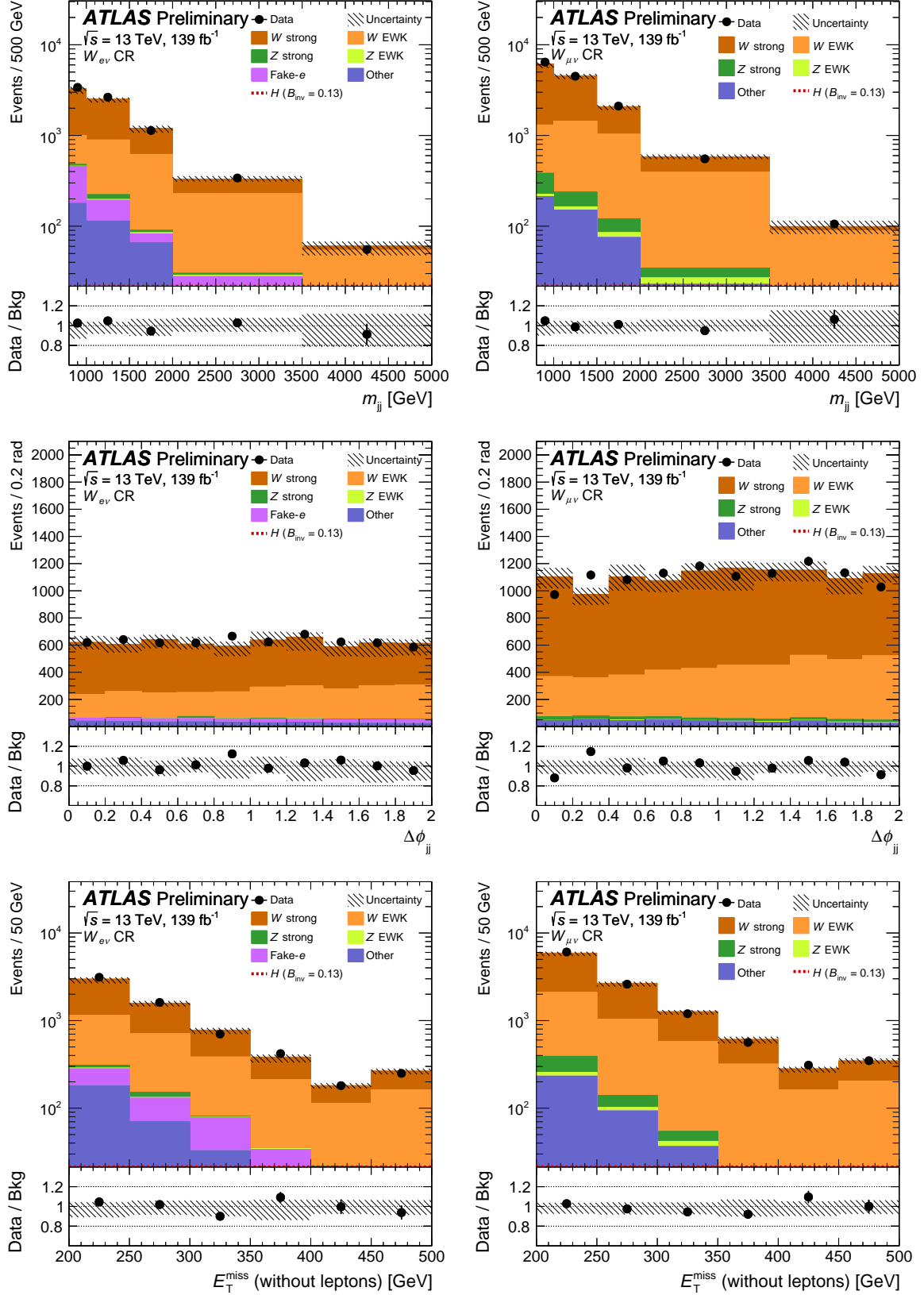
Figure 3.5: Distributions of m_{jj}, $\Delta\varphi_{jj}$, and E_T^{miss} (without leptons) in the $W_{e\nu}$ (left) and $W_{\mu\nu}$ (right) control regions. The simulation is normalised to cross-sections times luminosity and is shown prior to the likelihood fit. The small contribution from fake electrons is the expected contribution after the combined likelihood fit. Minor contributions from $t\bar{t}$, VV, VVV, and VBF H with $H \to \tau^+\tau^-$ or $H \to W^*W$ are summed up as "Other". The hatched band indicates statistical and reconstruction systematic uncertainties. [8]

3.5.3 Multijet Background

Background events from multijet processes tend to have large angles $\Delta\varphi_{jj}$ between the leading two jets and little E_T^{miss} originating from jet mis-measurements. The signal selection is designed to heavily suppress such events through the requirement of large E_T^{miss} and small $\Delta\varphi_{jj}$
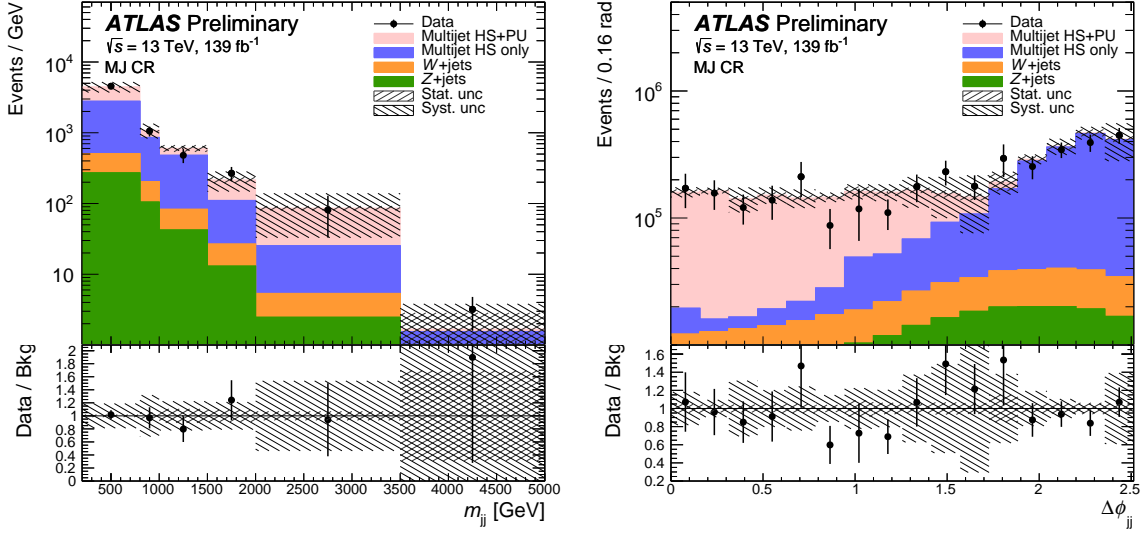
Figure 3.6: Distributions of m_{jj} and $\Delta\varphi_{jj}$ are shown in the MJ CR. The two multijet background components (HS only, blue) and (HS+PU, red) have been scaled to fit the observed $\Delta\varphi_{jj}$ distribution. The hatched bands indicate the statistical and the systematic uncertainties separately [8].

The multijet background is estimated from data using a modification to the "rebalance and smear" technique used in previous analyses [15] . As input to the method, an inclusive jet sample recorded by a set of single-jet triggers is used. Events are required to have no lepton candidate.

Each jet is next classified either as a hard-scatter (HS) jet or as a pile-up (PU) jet.The subset of events with two or more HS jets but no PU jet with $p_T > 25\,GeV$ define a HS-only sample, while the HS+PU sample contains events with two or more HS jets and exactly two PU jets with $p_T > 25\,GeV$ that are back-to-back ($\Delta\varphi_{jj} > 2.7$) and have an average p_T greater than $40\,GeV$. PU jets below the p_T threshold of $25\,GeV$ remain unchanged in this procedure.

The two multijet background components are normalised by a fit to the E_T^{miss} distribution in a loose multijet control region (MJ CR) with $E_T^{miss} > 100\,GeV$, $\Delta\varphi_{jj} < 2.5$, $\Delta\eta_{jj} > 2.5$, $m_{jj} > 200\,GeV$ and $p_T^{j3} < 25\,GeV$. The $\Delta\varphi_{jj}$ distribution is well suited for this, since HS topologies are expected to accumulate at large $\Delta\varphi_{jj}$, while at low $\Delta\varphi_{jj}$ the HS+PU topology should be dominant. The

shapes of the m_{jj} and $\Delta\varphi_{jj}$ distributions after the normalisation are shown in Fig. 3.6.

3.6 Systematic Uncertanties

sensitivety of an anlysis are generally affected and reduced by uncertanties generated by the Detector recontructions and simulations. two type of source of uncertanties an analysis has, Thoretical and experimental.

3.6.1 Theoretical Uncertanties

The theoretical uncertainties effects are originated from MC simulation of signal and background modelling. These uncertainties arise from fixed scale choices in the event generation, as well as the description of the initial-state PDF and parton showers.

The Z +jets and W +jets uncertanties assessed by varying the factoristation and the renormalisation scales , resummation and CKKW matching scales of The higher-order matrix element effects and parton shower, for strong V+jets and EW V+jets.The PDF uncertainties of the W and Z backgrounds are evaluated separately for each bin as the standard deviation of the 100 PDF replica of the NNPDF set.[8]

The VBF and ggF Higgs boson production inclusive cross-sections and uncertainties are provided by the LHC Higgs working group.

For the VBF process, there is an uncertainty due to the p_T-dependent NLO electroweak correction. This is estimated from HAWK to be 28%,The parton shower uncertainty for the VBF signal is estimated to range from 2% to 4% by comparing to a Powheg+Herwig 7 sample. PDF uncertainties assessed from the NNPDF set range from 1-2%.[8]

Uncertainties on the ggF process are also evaluated by renormalisation and factorization scale variations. A Stewart-Tackmann procedure is used to estimate the jet bin migration uncertainty. This gives a 45% uncertainty in the 2-jet bin and a 41% in the 3- and 4-jet bin. The smaller PDF and parton shower uncertainties are also included.[8]

3.6.2 Expirimental Uncertanties

This category encompasses the sources of systematic uncertainty from the calibration procedures of the detector and the LHC machine.

3.6.2.1 Luminosity

The integrated luminosity recorded by the ATLAS detector is known with a precision of 2.1,3.4,2.4,2.0% for 2015,2016,2017, and 2018 years of data taking. For the total dataset 2015-2018, the recommended uncertainty is 1.7%, which is applied.[8]

3.6.2.2 Trigger

systematic uncertainties have to be considered to account for possible trigger efficiency differences between data and simulation. This is done by comparing the combined L1+HLT trigger efficiency turn-on curve for simulated signal events with the turn-on curve derived from data using a sample recorded with single muon triggers.[8]

3.6.2.3 Electron and Muon Recontruction

Tools provided by the E/gamma combined performance group are used to estimate the systematic uncertainties related to electrons. We consider the uncertainty in the electron reconstruction and identification scale factors, and the energy scale and resolution. There is also an uncertainty on the inefficiency scale factor for the electron veto.[8]

Tools provided by the Muon combined performance group are used to estimate the systematic uncertainties related to muons. We consider the uncertainty in the muon efficiency factor, the isolation, and the momentum scale and resolution and the veto uncertanties .[8]

3.6.2.4 Jets and MET

Tools provided by the Jet/E_T^{miss} group for the jet energy scale (JES) and jet energy resolution (JER) uncertainties are used to evaluate this systematic uncertainty.[8]

Uncertainties on the reconstructed objects that go into the reconstruction of E_T^{miss} are propagated to the reconstruction of E_T^{miss} and are therefore not classified as "E_T^{miss} systematics" at the analysis level. The E_T^{miss} systematics come from the propagation of uncertainties on the soft track term scale and resolution and are provided by the METSystematicsTool.[8]

3.7   Results

When there is no excess of observed signal events , Upper limits often is setten for exclausion and interpretations using liklehood function based test .The upper limit on the branching ratio of the invisibly decaying Higgs boson is calculated using a maximum profiled likelihood fit . The limit is set at 95% CL using asymptotic formulae [17] for CLs [24] frequentist approach.

The signal strength μ is the one global free parameter of interest in the fit and represents the scale factor of the Higgs boson production cross section. For the signal, a Branching ratio of 100% is assumed. A fit to the observed data is done simultaneously for all CRs and SRs in each search bin (see Sec. 3.4.3) . The strong and electroweak components of the W+jets (Z+jets) backgrounds are scaled in each bin by the a normalisation factors , and motivated by lepton universality the electron and the muon CRs are combined for the $Z_{\ell\ell}$ CR. All systematic uncertainties are implemented as nuisance parameters $\vec{\theta}$.

The event yields in the eleven signal selection bins after the likelihood fit , and visualisation of the agreement in each CR and SR region bin is presented in Fig. 3.7.
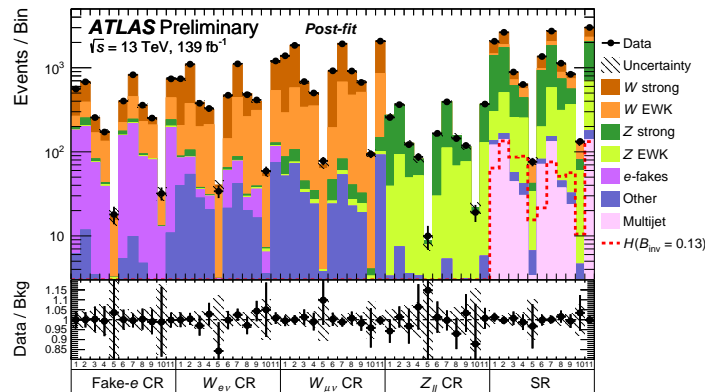

Figure 3.7: Post-fit results of all SR and CR bins. Minor contributions from $t\bar{t}$, VV, VVV, and VBF H with $H \rightarrow \tau^+\tau^-$ or $H \rightarrow W^*W$ are summed up as "Other' [8].

Overall, a good agreement of expected background yields and observed data is observed, and an upper limit on the branching ratio of the Higgs boson into invisible particles of 0.13 is set at 95% confidence level. This is in agreement with the expected value of $0.13^{+0.05}_{-0.04}$ (see Tab. 3.9).

Observed	Expected	$+1\sigma$	-1σ	$+2\sigma$	-2σ
0.132	0.132	0.183	0.095	0.248	0.071

Table 3.9: Expected and observed limits on $\mathcal{B}_{\text{inv}}$ for a Higgs boson with a mass of 125 GeV calculated at the 95% CL with 139 fb^{-1} [8].

this analysis shows a significant improvement. Figure 3.8 shows the m_{jj} and $\Delta\varphi_{jj}$ distributions after the likelihood fit in the inclusive signal region.
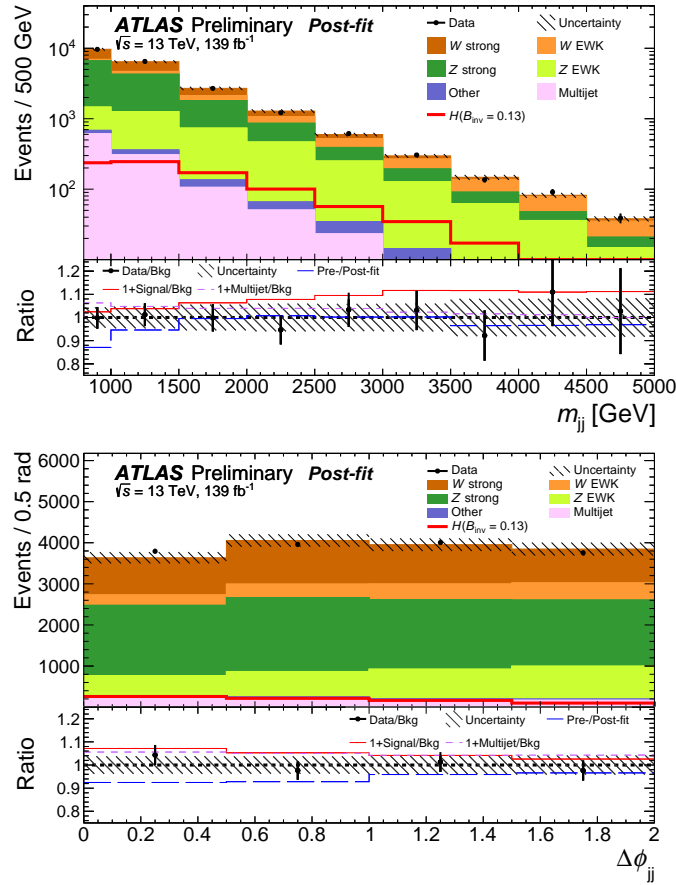

Figure 3.8: Post-fit m_{jj}(top) and $\Delta\varphi_{jj}$ (bottom) distribution in the inclusive signal region. Minor contributions from $t\bar{t}$, VV, VVV, and VBF H with $H \to \tau^+\tau^-$ or $H \to W^*W$ are summed up as "Other". [8]

The limit $\mathcal{B}_{\text{inv}}$ is related to a limit on the the spin-independent WIMP–nucleon cross sectionThis interpretation is compared to limits from some direct detection experiments in Fig. 3.9.To be comparable with the direct detection limits, the observed 90% CL upper limit on $\mathcal{B}_{\text{inv}}$ from this analysis of 11% is used.
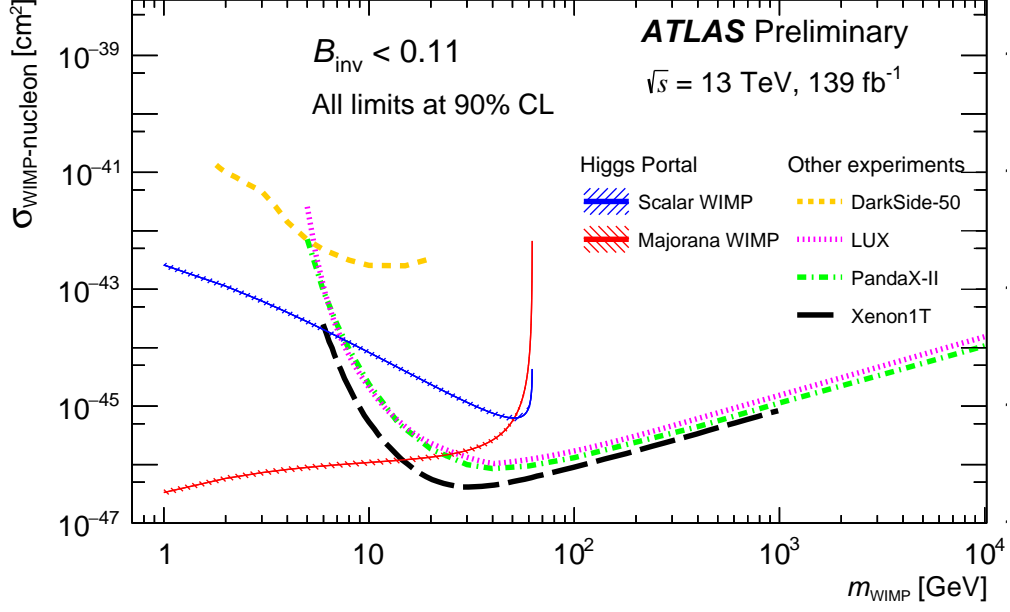
Figure 3.9: Upper limits on the spin-independent WIMP–nucleon cross section using Higgs portal interpretations of $\mathcal{B}_{\text{inv}}$ at 90% CL vs. m_{WIMP}. The plot shows results from Ref.[2, 18, 3, 1].

For the scalar WIMP interpretation, cross sections are excluded at values ranging from $\sim 3 \cdot 10^{-43}$ to $\sim 6 \cdot 10^{-46}\,\text{cm}^2$ for masses between $1\,GeV$ and $60\,GeV$. For the Majorana fermion WIMP interpretation the exclusion range is from $\sim 4 \cdot 10^{-47}$ to $\sim 10^{-45}\,\text{cm}^2$ for the same mass range.

Chapter 4

Statistical Combination of invisible Higgs decays

This chapter presents a recent result of Statistical Combination of searches for H $\rightarrow$ invisible decays where H is produced according to the Standard Model via vector boson fusion (VBF) or in association with a pair of top quarks in final states with zero or two leptons(t$\bar{t}$H).

4.1 Test Statistic in frequentist approach and CLs method

In particle physics experiments one often searches for processes that have been predicted but not yet seen, such as production of a Higgs boson. The statistical significance of an observed signal can be quantified by means of a p-value . It is useful to characterize the sensitivity of an experiment by reporting the expected (e.g., mean or median) significance that one would obtain for a variety of signal hypotheses.

4.1.1 Test Statistic for a discovrey of a positive signal

In this section we outline the general procedure used to search for a new phenomenon in the context of a frequentist statistical test [17]. For purposes of discovering a new signal process, one defines the null hypothesis, H_0, as describing only known processes, here designated as background. This is to be tested against the alternative H_1 , which includes both background as well as the sought after signal.

We perform the test statistic in Particle physics with the negative logarithm of the likelihood ratio defined by the likelihood function of some probability density functions (PDFs), here for signal and background. Suppose for each events in the signal sample one measures a variable x to contruct a histogramm $\mathbf{n} = (n_1, \ldots\ldots, n_N)$, the expectation value of n_i can be written

$$E[n_i] = \mu s_i + b_i \tag{4.1}$$

where the number of entries in ith bin of signal and background are

$$s_i = s_{tot} \int_{bini} f_s(x, \theta_s) dx \qquad b_i = b_{tot} \int_{bini} f_b(x, \theta_b) dx \tag{4.2}$$

Here the parameter μ determines the strength of the signal process, with $\mu = 0$ corresponding to the background-only hypothesis and $\mu = 1$ being the nominal signal hypothesis. The functions $f_s(x; \theta_s)$ and $f_b(x; \theta_b)$ are the probability density functions (pdfs) of the variable x for signal and background events, and θ_s and θ_b represent parameters that characterize the shapes of pdfs. The quantities s_{tot} and b_{tot} are the total mean numbers of signal and background events, and the integrals represent the probabilities for an event to be found in bin i Below we will use $\theta = (\theta_s, \theta_b, b_{tot})$ to denote as all so-called the nuisance parameters.

One often makes further subsidiary measurements that help constrain the nuisance parameters. For example, one may select a control sample where one expects mainly background events and from them construct a histogram of some chosen kinematic variable. This then gives a set of values $\mathbf{m} = (m, ..., m_M)$ for the number of entries in each of the M bins. The expectation value of mi can be written

$$E[m_i] = u_i(\theta) \tag{4.3}$$

Where the u_i are calculable quantities depending on the parameters θ. One often constructs this measurement so as to provide information on the background normalization parameter b_{tot} and also possibly on the signal and background shape parameters.

We define the likelihood function as the product of possion distribution in each bin like

$$L(\mu, \theta) = \prod_{j=1}^{N} \frac{(\mu s_j + b_j)^{n_j}}{n_j!} e^{-(\mu s_j + b_j)} \prod_{k=1}^{M} \frac{u_k^{m_k}}{m_k!} e^{-u_k} \tag{4.4}$$

To test a hypothesized value of μ we consider the profile likelihood ratio

$$\lambda(\mu) = \frac{L(\mu, \hat{\hat{\theta}})}{L(\hat{\mu}, \hat{\theta})} \tag{4.5}$$

Here $\hat{\hat{\theta}}$ in the numerator denotes the value of θ that maximizes L for the specified μ, i.e., it is the conditional maximum-likelihood (ML) estimator of θ (and thus is a function of μ).The denominator is the maximized (unconditional) likelihood function, i.e., $\hat{\mu}$ and $\hat{\theta}$ are their ML estimators.

A test statistic can be difined as the negative logarithm of the likelihood ratio $\lambda(\mu)$ as follows

$$t_\mu = -2\ln(\lambda(\mu)) \tag{4.6}$$

We may define a test of a hypothesized value of μ by using the statistic t_μ directly as measure of discrepancy between the data and the hypothesis, with higher values of t_μ correspond to increasing disagreement. To quantify the level of disagreement we compute the p-value,

$$p_\mu = \int_{t_{\mu,obs}}^{\infty} f(t_\mu | \mu) \, dt_\mu \tag{4.7}$$

where $t_{\mu,obs}$ is the value of the statistic t_μ observed from the data and $f(t_\mu | \mu)$ denotes the pdf of t_μ under the assumption of the signal strength μ.

In particle physics one usually converts the p-value into an equivalent signif-icance, Z, defined such that a Gaussian distributed variable found Z standard deviations above its mean has an upper-tail probability equal to p. That is,

$$Z = \Phi^{-1}(1 - p) \tag{4.8}$$

where Φ^{-1} is the quantile (inverse of the cumulative distribution) of the standard Gaussian. For a signal process such as the Higgs boson, the particle physics community has tended to regard rejection of the background hypothe-sis with a significance of at least Z = 5 as an appropriate level to constitute a discovery.

An important special case of the statistic t_μ described above is to test $\mu = 0$ in a class of model where we assume $\mu \geqslant 0$. Rejecting the $\mu = 0$ hypothesis effectively leads to the discovery of a new signal. For this important case we use the special notation q_μ . one sets

$$q_0 = \begin{cases} -2\ln(\lambda(\mu)) & \hat{\mu} \geqslant 0 \\ 0 & \hat{\mu} < 0 \end{cases} \tag{4.9}$$

where $\lambda < 0$ is the profile likelihood ratio for $\mu = 0$ as defined in Eq 4.6 . If the data fluctuate such that one finds fewer events than even predicted by background processes alone, then $\hat{\mu} < 0$ and one has $q_0 = 0$. As the event yield increases above the expected background, i.e., for increasing $\hat{\mu}$, one finds increasingly large values of q_0 , corresponding to an increasing level of incom-patibility between the data and the $\mu = 0$ hypothesis.

To quantify the level of disagreement between the data and the hypothesis of $\mu = 0$ using the observed value of q_0 we compute the p-value

$$p_0 = \int_{q_{0,obs}}^{\infty} f(q_0|0) \, dq_0 \tag{4.10}$$

4.1.2 Asimov Data

We define the Asimov data set such that when one uses it to evaluate the estimators for all parameters, one obtains the true parameter values. in previous exemple if we set $\nu_i = \mu s_i + b_j$ and then it's straighforward to evaluate the ML estimatos such .

$$\frac{\partial \ln L}{\partial \theta_j} = \sum_{i=1}^{N} \left(\frac{n_i}{\nu_i} - 1\right)\frac{\partial \nu_i}{\partial \theta_j} + \sum_{i=1}^{M} \left(\frac{m_i}{u_i} - 1\right)\frac{\partial u_i}{\partial \theta_j} \qquad (4.11)$$

This condition holds if the Asimov data, $n_{i,A}$ and $m_{i,A}$ are equal to their expectation values :

$$n_{i,A} = E[n_i] = \mu s_i(\theta) + b_i(\theta) \qquad (4.12)$$
$$m_{i,A} = E[m_i] = u_i(\theta) \qquad (4.13)$$

Here the parameter values represent those implied by the assumed distribution of the data. In practice, these are the values that would be estimated from the Monte Carlo model using a very large data sample.

4.1.3 CLs Method

This section provides a brief description of the CLs procedure [24] used for setting upper limits.. This is one of the three methods for setting limits , and has been widely used in HEP in recent years. The primary motivation for using CLs at this time in ATLAS is to allow for comparison with other experiments (CMS and Tevatron ...ect).

We assume that the analyst has constructed a test statistic q used to distinguish between the hypothesis that the data contain signal and background (s + b) and that of background only (b). These correspond to the distributions $f(q|s+b)$ and $f(q|b)$, as indicated in Figure 4.1.

Suppose the actual data result in a value q_{obs} of the test variable. The p-value of the (s+b) hypothesis is defined as the probability, under assumption of this hypothesis, to find a value of q with equal or lesser compatibility with the (s+b) model relative to what is found with q_{obs} . As the background-only distribution $f(q|b)$ is here shifted to the right,one takes the p-value of (s+b) to be the probability to find q greater than or equal to q_{obs} , under assumption of
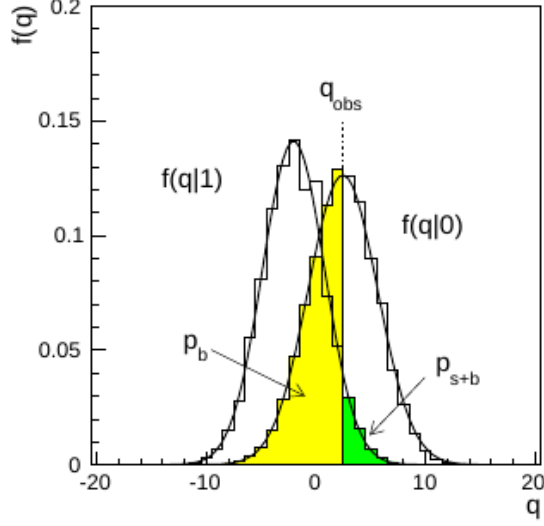
Figure 4.1: distrbution of the test variable q unde s+b and b hypotheses [24]

the (s+b) hypothesis

$$p_{s+b} = \int_{q_{obs}}^{\infty} f(q|s+b) \, dq \qquad (4.14)$$

In a similar way, one takes the p-value of the background-only hypothesis to be

$$p_b = \int_{-\infty}^{q_{obs}} f(q|b) \, dq \qquad (4.15)$$

In what is called the "CL_{s+b}" method, one carries out a standard statistical test of the (s+b) hypothesis based on its p-value, p_{s+b} . The signal model is regarded as excluded at a confidence level of $1 - \alpha = 95\%$ if one finds

$$p_{s+b} < \alpha \qquad (4.16)$$

where, e.g., $\alpha = 0.05$. A confidence interval at confidence level CL $= 1 - \alpha$ for the rate of the signal process can be constructed from those values of the rate s (or cross section) that are not excluded, and the upper limit s_{up} is the largest value of s not excluded. By construction, the interval $[0, s_{up}]$ will cover s with a probability of at least 95%, regardless of the value of s.

The problem with the CL_{s+b} procedure is that one will exclude, with probability close to α (i.e, 5%) hypotheses to which one has little or no sensitivity. This corresponds to the case where the expected number of signal events is much less than that of background.

To protect against excluding models to which one has little or no sensitivity, in the CLs procedure a signal model is regarded as excluded if one finds

$$CLs \equiv \frac{p_{s+b}}{1-p_b} < \alpha \qquad (4.17)$$

That is, the p-value is effectively penalized by dividing by $1 - p_b$. If the two distributions $f(q|b)$ and $f(q|s+b)$ are widely separated, then $1 - p_b$ is only slightly less than unity, the penalty is slight, and thus exclusion based in CLs is similar to that obtained from the usual p-value p_{s+b}. If, however, one has little sensitivity to the signal model, then the two distributions are close together, $1 - p_b$ becomes small, and thus the p-value of (s+b) is penalized (increased) more. In this way one is prevented from excluding signal models in cases of low sensitivity.

one can see that CLs is always greater than the p-value p_{s+b}. Thus the models excluded by requiring $CLs < \alpha$ are a subset of those excluded by the usual criterion $p_{s+b} < \alpha$, and the upper limit from CLs is therefore higher (weaker). In this sense the CLs procedure is conservative.

4.2 Statistical Combination of Higgs decays

In this chapter, we report the recent result of Statistical Combination of Invisbile Higgs decays of different channels.Three analyses contribute to the combination , two utilizing the full Run 2 dataset and the Run 1 H $\rightarrow$ invisible combination.

The signatures each Run 2 analysis addresses is shown in Figure 4.2 . Each analysis final state is characterised by large value of E_T^{miss} corresponding to the invisible decay of the Higgs boson and additional physics objects to target a specific Higgs boson production mode.

We summarize the analysis strategy of each input analysis - VBF+E_T^{miss}, $t\bar{t} + E_T^{miss}$(two final states: all-hadronic) and the Run 1 H $\rightarrow$ invisible combination .

The VBF+$E_T^{miss} + \gamma$, jet+E_T^{miss} , $(Z \rightarrow)ll + E_T^{miss}$ and $(W \rightarrow)ll + E_T^{miss}$ analyses were considered for inclusion but ultimately rejected due to timeline constraints.
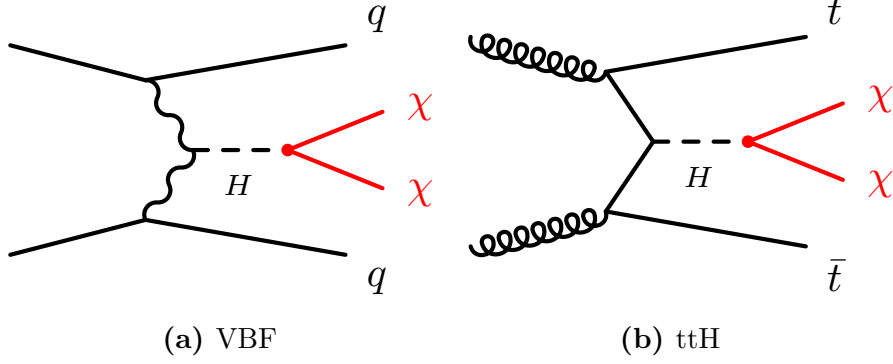
(a) VBF   **(b)** ttH

Figure 4.2: Feynman diagrams showing the signals for each input Run 2 analysis [5].

.

4.2.1   VBF $+E_T^{miss}$

The VBF analysis is designed for sensitivity to $\mathcal{B}_{H\to inv}$. The signal, as shown
in figure 4.2a, is characterized by two "VBF" jets with a wide separation in
pseudorapidity and missing energy from the invisible Higgs decay. A full list
of signal region selections are provided in Section 3.4.3. This analysis observes
(expects) an upper limit on $\mathcal{B}_{H\to inv}$ of 0.13 $(0.13^{+0.05}_{-0.04})$ at the 95% CL.

4.2.2   VBF Workspace Validation

Fits are performed on the observed data in the workspace. A stable minimum
is found at $\mu_{sig} = 0.000 \pm 0.068$ using an unconditional maximum Likelihood
fit. The pulls, constraints, and impacts on the best-fit value of the POI ($\hat{\mu}_{sig}$)
of the nuisance parameters are shown in Figure 4.3 for both the original anal-
ysis and the version produced with the statistics tools used for the combination.

The effects look very similar between the two plots, some minor differences
in impact rankings could be due to difference in fitting configurations.

Expected and observed limits can be found in Table 4.1. The results are
reproduced and match very well with what were reported by the VBF analysis.
The correlation of the fitting parameters is shown in Figure 4.4, and the
distribution of the observed negative Log-Likelihood (NLL) ratio as a function
of μ_{sig} is shown in Figure 4.5. The observed limit can also be interpreted in the
NLL plot of Figure 4.5.
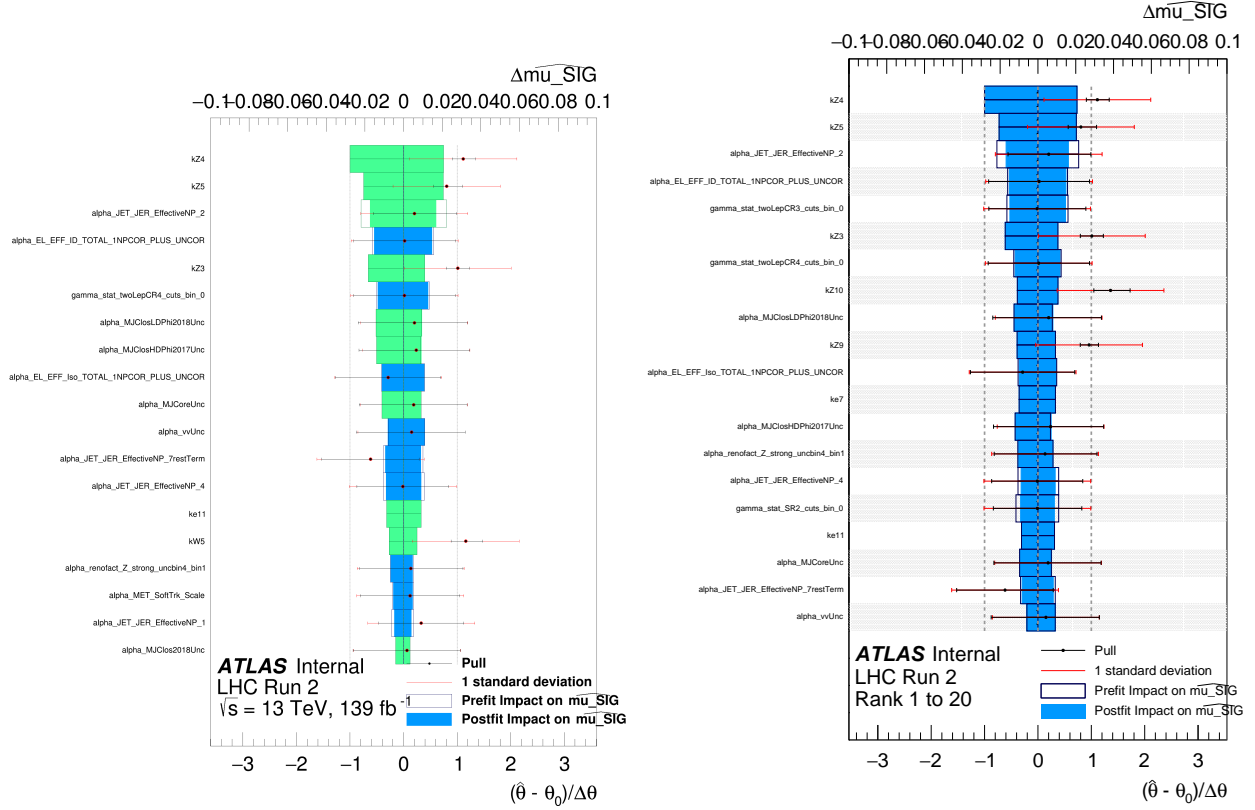
(a) Valided pull-constraint-impact ranking **(b)** The origine pull-constraint-impact ranking

Figure 4.3: Nuisance parameter values and impacts on $\hat{\mu}_{sig}$ of the nuisance parameters in the VBF workspace. 4.3a: version produced with the statistics tools used in for the combination; blue (green) colour indicates positive (negative) correlation with μ_{sig}. 4.3b: version produced by the individual analysis [25]. Only 20 parameters with the highest ranked post-fit impact on $\hat{\mu}_{sig}$ are shown. The ke* parameters are normalisation factors for estimating fake electrons in the WCRs of VBF analysis

Analysis	Median expected	$\pm 1\sigma$	$\pm 2\sigma$	Observed
our code	0.131	0.181 0.094	0.244 0.070	0.130
published [8]	0.132	0.183 0.095	0.248 0.071	0.132

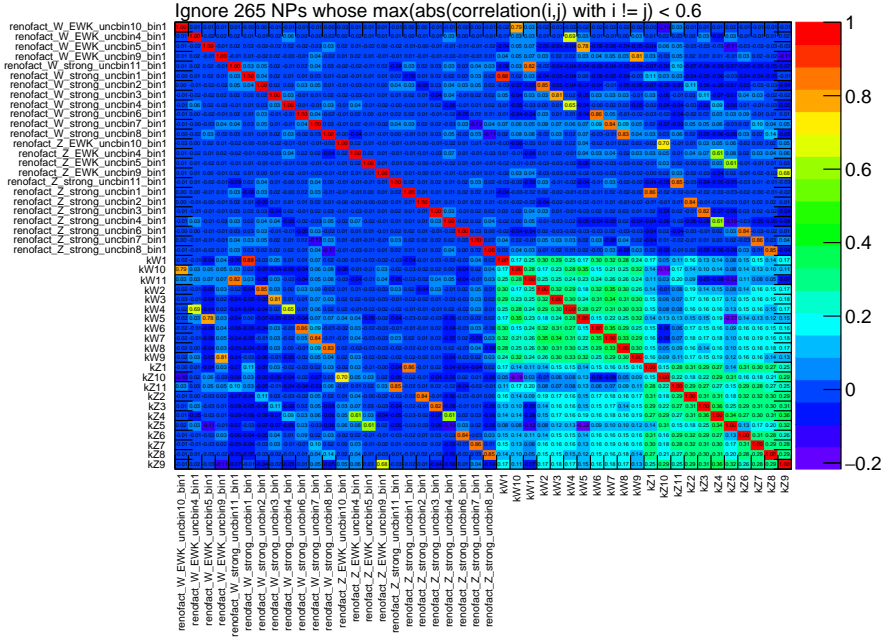**Table 4.1:** 95% CL expected and observed (CLs) limits for the single VBF analysis validation.

Figure 4.4: Correlations between fitting parameters in the VBF workspace extracted from a fit to data. Only the parameters which have at least an absolute correlation value (not with itself) > 0.6 are shown. This plot was made by Hinv team.
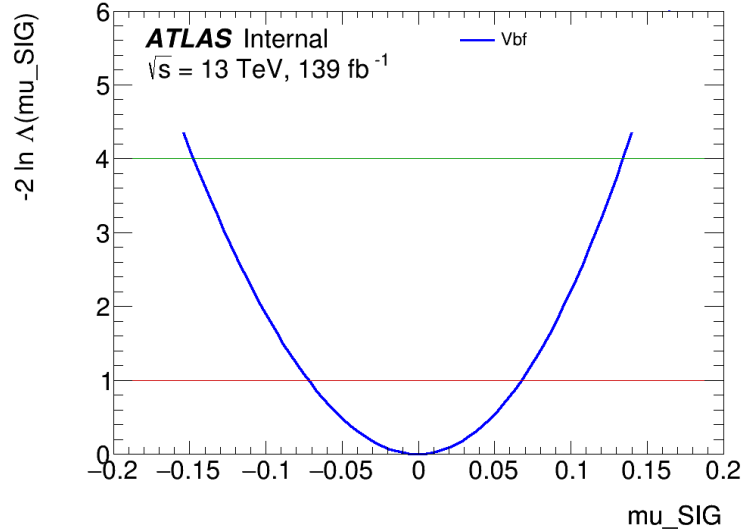

Figure 4.5: Distribution of (two times) the negative Log-Likelihood ratio over $\hat{\mu}_{sig}$ for VBF. The horizontal distance from $\hat{\mu}_{sig}$ to the crossing point with the red (green) line shows the 1σ (2σ) deviation from $\hat{\mu}_{sig}$. The curve has been obtained from fit to the unblinded data.

4.2.3 $t\bar{t} + E_T^{miss}$

The production mode of the Higgs boson in association with top quark pairs is targeted by reinterpreting two searches for new phenomena in association with heavy flavour quarks. The final states arising from this production mode are characterised by the presence of b-tagged jets and different charged lepton multiplicities, depending on the decay mode of the two W bosons from the $t\bar{t}$ decays, in addition to E_T^{miss} coming from the invisible decay products of the Higgs boson and from neutrinos.There two analysis contributed to this result $ttH0l$ and $ttH2l$

The first analysis ttHol [7] targeting the $t\bar{t}H$ topology is optimised to search for scalar partners of the top quark (top squarks) and considers the all-hadronic decay mode of the $t\bar{t}$ system by selecting events collected with the E_T^{miss}trigger with no reconstructed leptons. Furthermore, the presence of at least two b-tagged jets and $E_T^{miss} > 250$ GeV, to attain full trigger efficiency, are required. Four signal regions (SR) are then defined to address different kinematic regions depending on the mass spectrum of the supersymmetric particles considered.

The second analysis ttH2l [9] is a search for new physics in events with two opposite-charge leptons (electrons or muons), jets and missing transverse momentum, exploiting events collected with dileptonic triggers. The event selection is designed specifically to address DM models in which a spin-0 mediator particle (here the SM Higgs boson) is created in association with $t\bar{t}$ and couples directly to DM.

When interpreting the analyses as $H \rightarrow inv$ searches, the individual observed (expected) limits on $\mathcal{B}_{inv}$ at the 95% CL in the $t\bar{t}H0l$ and in the $t\bar{t}H2l$ channels are 0.94 ($0.64^{+0.29}_{-0.19}$) and 0.37 ($0.42^{+0.19}_{-0.12}$), respectively.

4.2.4 $t\bar{t}$ Workspace Validation

The workspace used is provided by the ttH combination effort , and includes input from 2L, and 0L high-MET. Fits are performed on the observed data in the workspace because the included channels are already unblinded. A minimum is found at $\mu_{sig} = 0.025 \pm 0.190$.

The pulls, constraints and impacts on $\hat{\mu}_{sig}$ of the nuisance parameters are shown in Figure 4.6
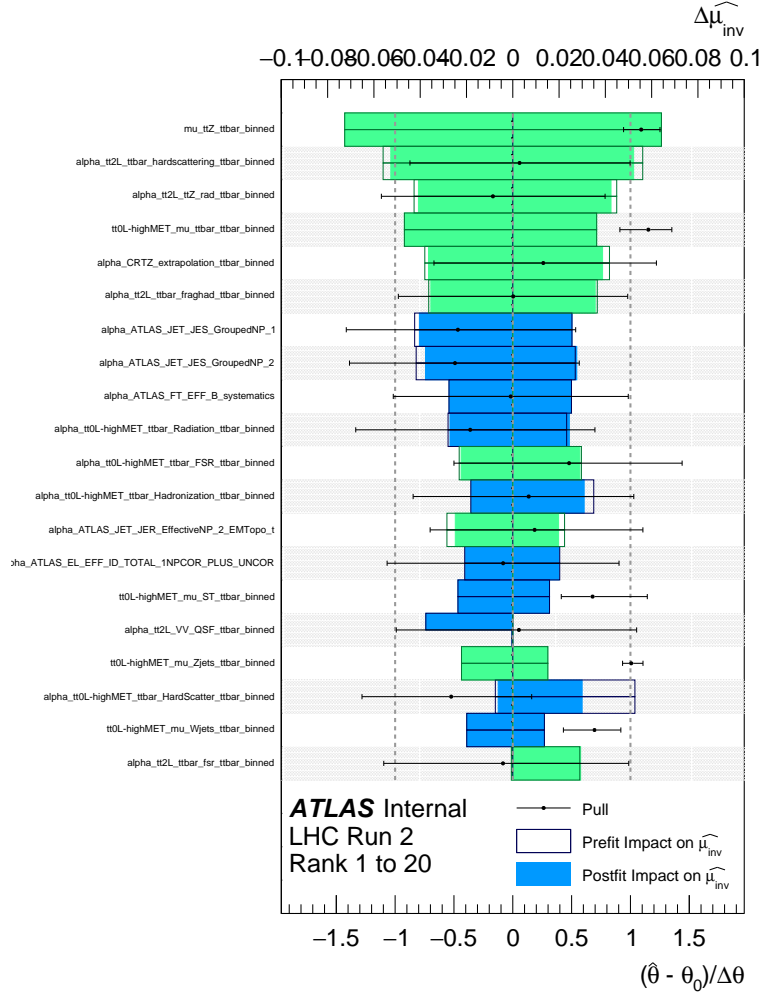
Figure 4.6: Pulls, constraints and impacts on $\hat{\mu}_{sig}$ of the nuisance parameters in the *ttH* workspace. Only 20 parameters with the highest ranked post-fit impact on $\hat{\mu}_{sig}$ are shown. Blue (green) colour indicates positive (negative) correlation. This plot was made by Hinv team.

Expected and observed limits can be found in Table 4.2. The limit values agree very well between our produced results and the individual analysis.

Analysis	Median expected	$\pm 1\sigma$	$\pm 2\sigma$	Observed
our code	0.360	0.502 0.259	0.684 0.193	0.402
reference from analysis team	0.360	0.509 0.258	0.697 0.191	0.400

Table 4.2: 95% CL expected and observed (CLs) limits for the single ttH analysis validation. Very tiny discrepancies are seen due to different tools are used for CLs limit calculation (our HCombTool `quickFit` vs analysis tool `pyhf`).

The correlation of the fitting parameters is shown in Figure 4.7, the distribution of the negative Log-Likelihood (NLL) ratio as a function of μ_{sig} is shown in Figure 4.8. The mentioned plots were produced by the combination effort.
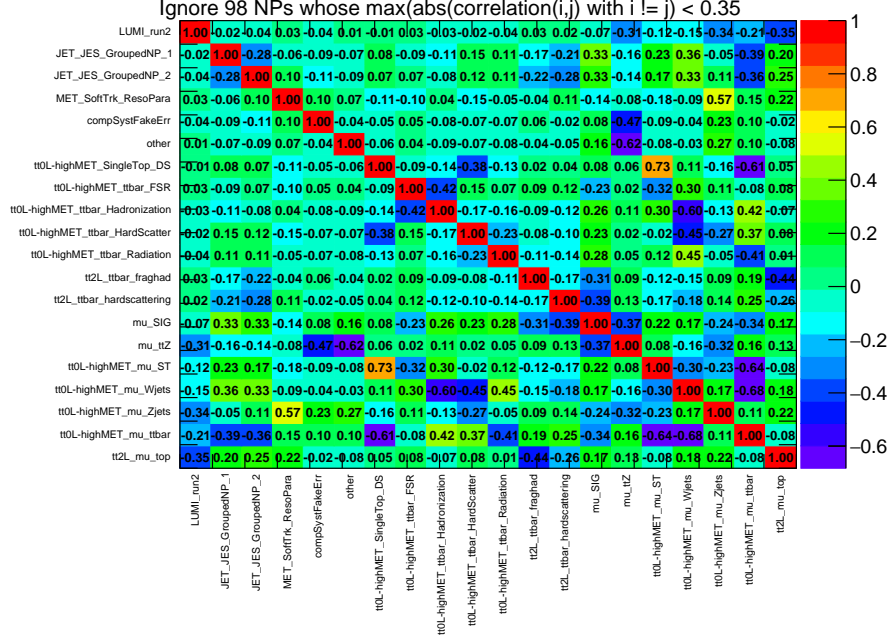
Figure 4.7: Correlations between fitting parameters in the ttH workspace. Only the parameters which have at least an absolute correlation value (not with itself) > 0.35 are shown. This plot is made by hinv team.
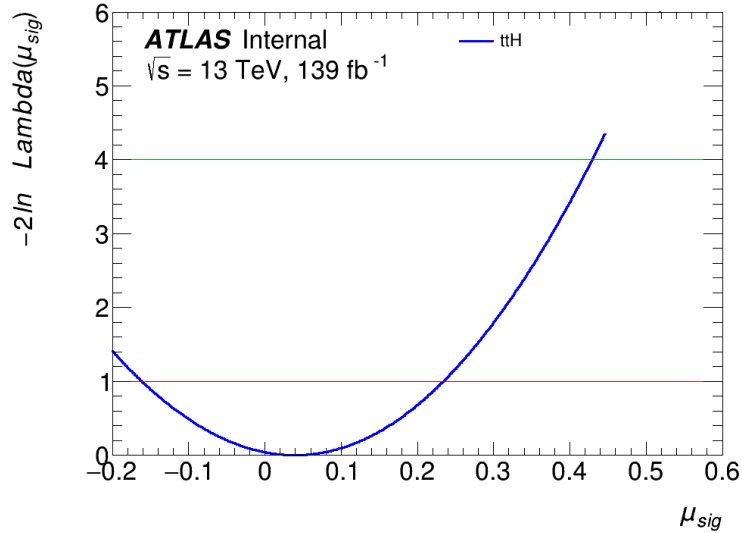

Figure 4.8: Distribution of (two times) the negative Log-Likelihood ratio over μ_{sig} for ttH. The horizontal distance from μ_{sig} to the crossing point with the red (green) line shows the 1σ (2σ) deviation from μ_{sig}. The curve has been obtained from fit to the unblinded data. This plot is made by hinv team.

4.2.5 Run 1 Combination

The Run 1 ATLAS $H \to inv$ combination utilised 4.7 fb^{-1} of pp collision data at $\sqrt{s} = 7$ TeV and 20.3 fb^{-1} at $\sqrt{s} = 8$ TeV This combination considers inputs from direct searches of $H \to inv$ through Higgs bosons produced via VBF or in association with a vector boson V, where the vector boson decays either leptonically ($Z \to ll$) or hadronically ($W/Z \to jj$). All the signal regions and control regions are used to perform a maximum-likelihood fit resulting in an observed (expected) upper limit of $\mathcal{B}_{H \to inv} < 0.25$ ($0.27^{+0.10}_{-0.08}$) at the 95% CL. In a similar way to Run 2, the sensitivity is driven by the VBF channel.

4.2.6 Statistical Model

The statistical combination of the analyses is performed by constructing the product of their likelihoods and maximizing the resulting likelihood ratio [17]:

$$\Lambda(\alpha; \theta) = \frac{L\left(\alpha, \hat{\hat{\theta}}(\alpha)\right)}{L\left(\hat{\alpha}, \hat{\theta}\right)}$$

where α and θ are respectively the parameter of interest and the nuisance parameters. In the numerator, the nuisance parameters are set to their profiled values $\hat{\hat{\theta}}(\alpha)$, which maximise the likelihood function for fixed values of the parameter of interest α. In the denominator, both the parameter of interest and the nuisance parameters are set to the values $\hat{\alpha}$ and $\hat{\theta}$ respectively which jointly maximise the likelihood. with $\mathcal{B}_{H \to inv}$ as the parameter of interest α. Systematic uncertainties are modelled in the likelihood function as nuisance parameters θ constrained by Gaussian or log-normal probability density functions [6]. Expected results are obtained using the Asimov dataset technique [17]. In absence of a significant excess, upper limits on $\mathcal{B}_{H \to inv}$ are provided following the CL_s formalism [24] using the profile likelihood ratio as a test statistic. In the following, several combinations will be discussed with an increasing number of input analyses:

- combination of $t\bar{t}H2l$ and $t\bar{t}H0l$ searches in Run 2

- combination of ttH and VBF searches in Run 2

- combination of Run 2 and Run 1 results

4.3 Results

The negative logarithmic profile likelihood ratios $-2\,\Delta\ln(\Lambda)(\mathcal{B}_{inv}; \theta)$ as a function of $\mathcal{B}_{H\to inv}$ of the individual analyses and of their combination are shown in Fig. 4.9 (a). The result of the combination of the ttH0l and ttH2l analyses is reported in Table 4.3. The best-fit values of $\mathcal{B}_{H\to inv}$ of the individual analyses are compatible within one standard deviation and the combination yields a value of 0.04 ± 0.20. The combined observed 95% CL upper limit on $\mathcal{B}_{H\to inv}$ is 0.40 while the expected value is $0.36^{+0.15}_{-0.10}$. The combination improves the sensitivity of the ttH2l analysis by 15%. The overall uncertainty is dominated by the limited statistics of the data and to a smaller extent by background modelling and JES uncertainties.
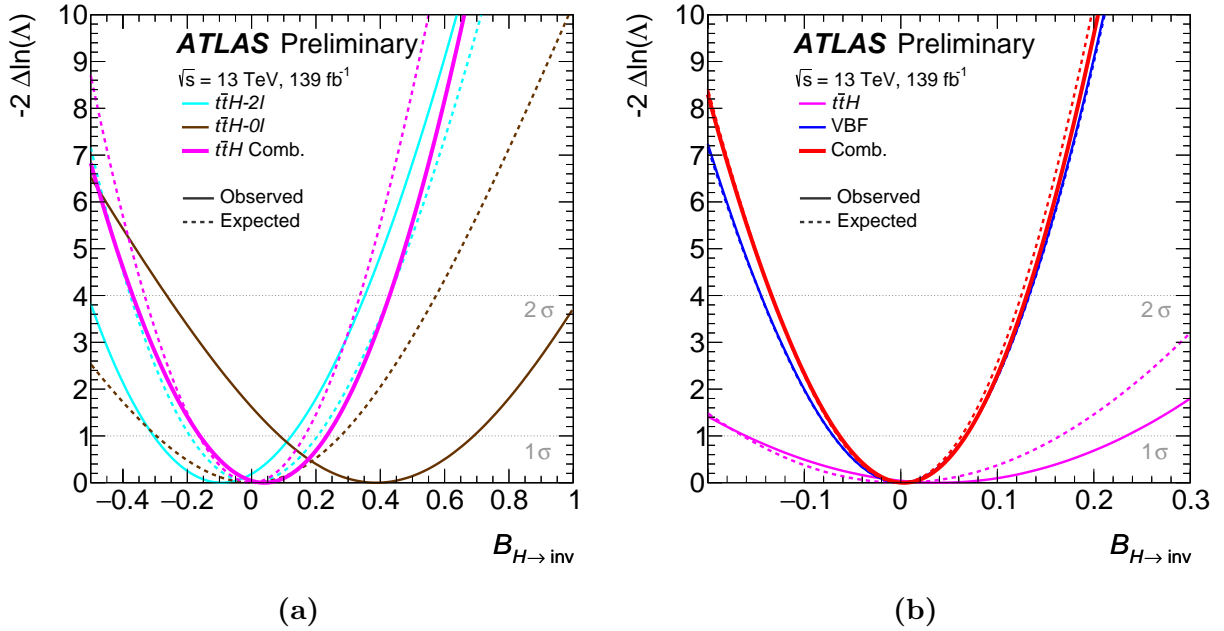

Figure 4.9: The expected and observed negative logarithmic profile likelihood ratio $-2\,\Delta\ln(\Lambda)$ as a function of $\mathcal{B}_{H\to inv}$ for the $t\bar{t}H0l$ and $t\bar{t}H2l$ analyses and their statistical combination (a). The expected and observed likelihood profiles for the statistical combination in the ttH topology from (a), the $H \to inv$ search in the VBF topology, and their statistical combination (b). All searches use 139 fb^{-1} of Run 2 data. [5]

Analysis	Best fit $\mathcal{B}_{inv}$	Observed upper limit	Expected upper limit	Reference
ttH0l	0.39 ± 0.30	0.94	$0.64^{+0.29}_{-0.19}$	[7]
ttH2l	$-0.09^{+0.22}_{-0.21}$	0.37	$0.42^{+0.19}_{-0.12}$	[9]
$t\bar{t}H$ comb.	0.04 ± 0.20	0.40	$0.36^{+0.15}_{-0.10}$	this Document

Table 4.3: Summary of results from direct searches for invisible decays of the 125 GeV Higgs boson in the ttH topology using 139 fb^{-1} of Run 2 data, and their statistical combination. Shown are the best-fit values of $\mathcal{B}_{H \to inv}$, as well as observed and expected upper limits on $\mathcal{B}_{H \to inv}$ at the 95% CL. [5]

4.3.1 Run 1 + Run 2 Combination

The Run 2 combination consiste of ttHcomb and VBF, while the VBF is most sensetive one. The negative logarithmic profile likelihood ratios $-2\,\Delta\ln(\Lambda)(\mathcal{B}_{inv}; \theta)$ as a function of $\mathcal{B}_{H \to inv}$ of the individual analyses and of the combined Run 2 result are shown in Fig. 4.9 (b), corresponding to a best-fit combined value of $\mathcal{B}_{H \to inv} = (0.00^{+0.06}_{-0.07})$.

In the absence of a significant excess, an upper limit at the 95% CL of $\mathcal{B}_{H \to inv} < 0.13(0.12^{-0.05}_{-0.04})$ is observed (expected). With respect to the most sensitive single analysis, the VBF Run 2 result, the Run 2 combination brings a relative sensitivity improvement of 5%.

The observed $-2\,\Delta\ln(\Lambda)(\mathcal{B}_{H \to inv}; \theta)$ of the combined Run 1+2 result is represented in Fig. 4.10, alongside the individual Run 1 and Run 2 combinations. A best-fit value of $\mathcal{B}_{inv} = 0.00 \pm 0.06$ is obtained for the Run 1+2 combination, corresponding to an observed (expected) upper limit of $\mathcal{B}_{inv} < 0.11(0.11^{+0.04}_{-0.03})$ at 95% CL. The final result, together with the results in the individual Run 2 analyses as well as the Run 2-only and the Run 1-only combinations, are summarized in Table 4.4, and the upper limits on $\mathcal{B}_{inv}$ are graphically represented in Fig. 4.11. The Run 1+2 combination reaches a relative sensitivity improvement of 15% with respect to the results of the VBF Run 2 analysis, which is the most sensitive input of the combination.
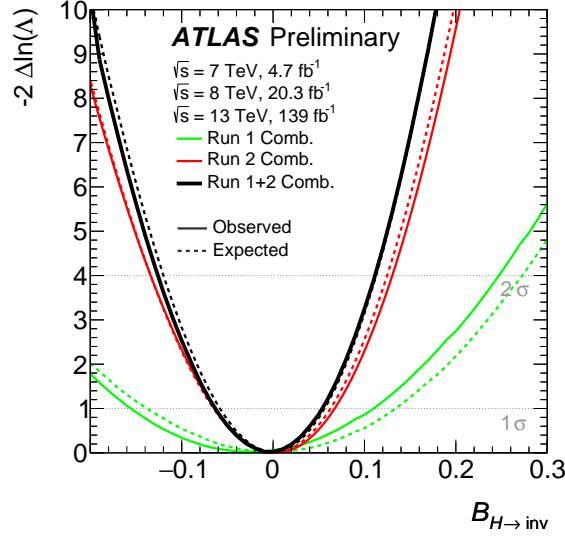
Figure 4.10: The expected and observed negative logarithmic profile likelihood ratios $-2\,\Delta\ln(\Lambda)$ as a function of $\mathcal{B}_{H\to inv}$ for the combined results using Run 1 and Run 2 alone, together with their combination. [5]

Analysis	$\sqrt{s}$ [TeV]	Int. luminosity $[fb^{-1}]$	Best fit B_{inv}	Observed upper limit	Expected upper limit	Reference
Run 2 VBF	13	139	$0.00^{+0.07}_{-0.07}$	0.13	$0.13^{+0.05}_{-0.04}$	[8]
Run 2 ttH	13	139	$0.04^{+0.20}_{-0.20}$	0.40	$0.36^{+0.15}_{-0.10}$	This document
Run 2 Comb.	13	139	$0.00^{+0.06}_{-0.07}$	0.13	$0.13^{+0.05}_{-0.04}$	This document
Run 1 Comb.	7, 8	4.7, 20.3	$-0.02^{+0.14}_{-0.13}$	0.25	$0.27^{+0.10}_{-0.08}$	[6]
Run 1+2 Comb.	7, 8, 13	4.7, 20.3, 139	$0.00^{+0.06}_{-0.06}$	0.11	$0.11^{+0.04}_{-0.03}$	This document

Table 4.4: Summary of results from direct searches for invisible decays of the 125 GeV Higgs boson and their statistical combinations. Shown are the best-fit values of $\mathcal{B}_{inv}$, as well as observed and expected upper limits on $\mathcal{B}_{inv}$ at the 95% CL.[5]
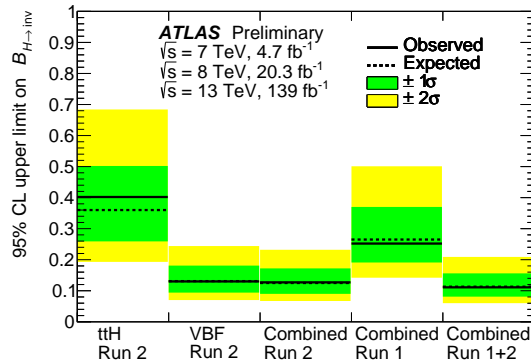

Figure 4.11: The observed and expected upper limits on $\mathcal{B}_{inv}$ at the 95% CL from direct searches for invisible decays of the 125 GeV Higgs boson and their statistical combinations in Run 1 and 2. The 1σ and 2σ uncertainty bands on the expected limits are shown as green and yellow, respectively. [5]

70

4.4 Compariason to to direct dark matter detection expirements

The constraint from the combined observed Run 1+2 exclusion limit of $\mathcal{B}_{inv} < 0.09$ at 90% CL is compared to the results from representative direct DM detection experiments in Fig. 4.12. This comparison is performed in the context of Higgs portal models. The translation of the $\mathcal{B}_{inv}$ result into a weakly interacting massive particle (WIMP)-nucleon scattering cross-section σ_{WIMP-N} relies on an EFT appoach
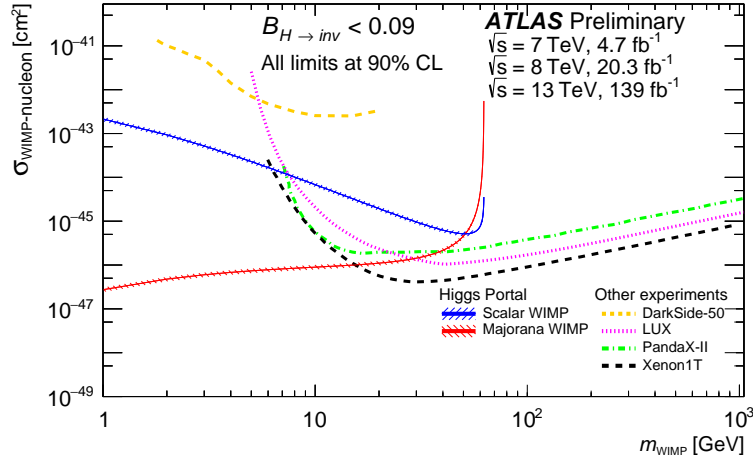

Figure 4.12: Comparison of the upper limits at 90% CL from direct detection experiments on the spin-independent WIMP-nucleon scattering cross-section to the observed exclusion limits from this analysis, as a function of the WIMP mass. [5]

The excluded σ_{WIMP-N} values range down to 10^{-45} cm^2 in the scalar WIMP scenario. In the Majorana fermion WIMP case exclusions of σ_{WIMP-N} ranges from values down to 2×10^{-47} cm^2.

General Conclusion

This Manuscript has presented a search for dark matter production via VBF using 139 fb^{-1} of pp collision data at $\sqrt{s} = 13$ TeV . No evidence of such production was found; the Standard Model predictions describe the data accurately to well within the uncertainties. This was interpreted in terms of a SM Higgs mediator, and an upper limit of 13% was placed on its invisible branching ratio at a 95% confidence interval. This limit was used to place constraints on the DM-nucleon scattering cross section within the context of an effective field theory, in order to draw comparisons with direct detection experiments.and we statistically combined the VBF and ttH topologies assuming SM-like Higgs boson production. An upper limit on the invisible Higgs boson branching ratio of $\mathcal{B}_{H \to inv} < 0.13(0.12^{+0.05}_{-0.04})$ is observed (expected) at the 95% CL. A statistical combination of this result with the combination of direct H$\to inv$ searches using up to 4.7 fb^{-1} of pp collision data at $\sqrt{s} = 7 \ TeV$ and up to 20.3 fb^{-1} at 8 TeV collected in Run 1 of the LHC yields an observed (expected) upper limit of $\mathcal{B}_{H \to inv} < 0.11(0.11^{+0.04}_{-0.03})$ at the 95% CL. The combined Run 1+2 result is translated into upper limits on the WIMP-nucleon scattering cross-section for Higgs portal models.

Through out this manuscript, We start by giving an overview of the Standard model as the main theory of LHC experiments, and The channels of Higgs production invstigated by LHC. and in the next chapter we outline one of the simplest models of DM detection especially in colliders, known as Vector DM of Higgs portal models, and then we showed the working analyses interpreting thoses models. and we moved to next part where we reviewed the VBF analysis and it's strategy for hunting the DM signal. and we end the manuscript by the last result of Higgs invisible combination of all DM channels and interpret the result as an exclausion limit of the Higgs branching ratio in WIMPs-nucleon cross section and WIMP mass phase space in EFT Higgs portal model and we compare it with different direct detection expiremets.

Bibliography

[1] P. Agnes et al. "Low-Mass Dark Matter Search with the DarkSide-50 Experiment". In: *Phys. Rev. Lett.* 121.8 (2018), p. 081307. DOI: 10.1103/PhysRevLett.121.081307. arXiv: 1802.06994 [astro-ph.HE].

[2] D. S. Akerib et al. "Results from a search for dark matter in the complete LUX exposure". In: *Phys. Rev. Lett.* 118.2 (2017), p. 021303. DOI: 10.1103/PhysRevLett.118.021303. arXiv: 1608.07648 [astro-ph.CO].

[3] E. Aprile et al. "Dark Matter Search Results from a One Ton-Year Exposure of XENON1T". In: *Phys. Rev. Lett.* 121.11 (2018), p. 111302. DOI: 10.1103/PhysRevLett.121.111302. arXiv: 1805.12562 [astro-ph.CO].

[4] Giorgio Arcadi, Abdelhak Djouadi, and Marumi Kado. "The Higgs-portal for vector Dark Matter and the Effective Field Theory approach: a reappraisal". In: *Phys. Lett. B* 805 (2020), p. 135427. DOI: 10.1016/j.physletb.2020.135427. arXiv: 2001.10750 [hep-ph].

[5] ATLAS Collaboration. *Combination of searches for invisible Higgs boson decays with the ATLAS experiment.* ATLAS-CONF-2020-069. 2020. URL: %7Bhttp://cds.cern.ch/record/2740927%7D.

[6] ATLAS Collaboration. "Constraints on new phenomena via Higgs boson couplings and invisible decays with the ATLAS detector". In: *JHEP* 11 (2015), p. 206. DOI: 10.1007/JHEP11(2015)206. arXiv: 1509.00672 [hep-ex].

[7] ATLAS Collaboration. "Search for a scalar partner of the top quark in the all-hadronic $t\bar{t}$ plus missing transverse momentum final state at $\sqrt{s} = 13$ TeV with the ATLAS detector". In: *Eur. Phys. J. C* 80 (2020), p. 737. DOI: 10.1140/epjc/s10052-020-8102-8. arXiv: 2004.14060 [hep-ex].

[8] ATLAS Collaboration. *Search for invisible Higgs boson decays with vector boson fusion signatures with the ATLAS detector using an integrated luminosity of 139 fb^{-1}.* ATLAS-CONF-2020-008. 2020. URL: %7Bhttps://atlas.web.cern.ch/Atlas/GROUPS/PHYSICS/CONFNOTES/ATLAS-CONF-2020-008%7D.

[9] ATLAS Collaboration. *Search for new phenomena in events with two opposite-charge leptons, jets and missing transverse momentum in pp collisions at $\sqrt{s} = 13$ TeV with the ATLAS detector.* ATLAS-CONF-2020-046. 2020. URL: https://cds.cern.ch/record/2728056.

[10] ATLAS Collaboration. "Search for the Standard Model Higgs boson in the decay channel $H \to ZZ^{(*)} \to 4ll$ with the ATLAS detector". In: *Phys. Lett. B* 705 (2011), p. 435. DOI: 10.1016/j.physletb.2011.10.034. arXiv: 1109.5945 [hep-ex].

[11] ATLAS Collaboration. "Search for the Standard Model Higgs boson in the two photon decay channel with the ATLAS detector at the LHC". In: *Phys. Lett. B* 705 (2011), p. 452. DOI: 10.1016/j.physletb.2011.10.051. arXiv: 1108.5895 [hep-ex].

[12] Seungwon Baek, P. Ko, and Wan-Il Park. "Invisible Higgs Decay Width vs. Dark Matter Direct Detection Cross Section in Higgs Portal Dark Matter Models". In: *Phys. Rev. D* 90.5 (2014), p. 055014. DOI: 10.1103/PhysRevD.90.055014. arXiv: 1405.3530 [hep-ph].

[13] E. Behnke et al. "Final Results of the PICASSO Dark Matter Search Experiment". In: *Astropart. Phys.* 90 (2017), pp. 85–92. DOI: 10.1016/j.astropartphys.2017.02.005. arXiv: 1611.01499 [hep-ex].

[14] Matteo Cacciari, Gavin P. Salam, and Gregory Soyez. "The anti-k_t jet clustering algorithm". In: *JHEP* 04 (2008), p. 063. DOI: 10.1088/1126-6708/2008/04/063. arXiv: 0802.1189 [hep-ph].

[15] CMS Collaboration. "Search for New Physics with Jets and Missing Transverse Momentum in pp collisions at $\sqrt{s} = 7\,\text{TeV}$". In: *JHEP* 08 (2011), p. 155. DOI: 10.1007/JHEP08(2011)155. arXiv: 1106.4503 [hep-ex].

[16] CMS Collaboration. "Search for the standard model Higgs boson decaying to W^+W^- in the fully leptonic final state in pp collisions at $\sqrt{s} = 7\,\text{TeV}$". In: *Phys. Lett. B* 710 (2012), p. 91. DOI: 10.1016/j.physletb.2012.02.076. arXiv: 1202.1489 [hep-ex].

[17] Glen Cowan et al. "Asymptotic formulae for likelihood-based tests of new physics". In: *Eur. Phys. J. C* 71 (2011), p. 1554. DOI: 10.1140/epjc/s10052-011-1554-0. arXiv: 1007.1727 [physics.data-an]. Erratum: Eur. Phys. J. C **73** (2013) 2501.

[18] Xiangyi Cui et al. "Dark Matter Results From 54-Ton-Day Exposure of PandaX-II Experiment". In: *Phys. Rev. Lett.* 119.18 (2017), p. 181302. DOI: 10.1103/PhysRevLett.119.181302. arXiv: 1708.06917 [astro-ph.CO].

[19] Abdelhak Djouadi et al. "Direct detection of Higgs-portal dark matter at the LHC". In: *Eur. Phys. J. C* 73.6 (2013), p. 2455. DOI: 10.1140/epjc/s10052-013-2455-1. arXiv: 1205.3169 [hep-ph].

[20] Abdelhak Djouadi et al. "Implications of LHC searches for Higgs–portal dark matter". In: *Phys. Lett. B* 709 (2012), pp. 65–69. DOI: 10.1016/j.physletb.2012.01.062. arXiv: 1112.3299 [hep-ph].

[21] EL HASSAN SAIDI. *Introduction to Standard Model of Electro-Weak Interactions*. EL.H.SAIDI MOHAMED V UNIVERSITY RABAT LPHE-MS. 2017.

[22] Michio Kaku. *Quantum Field Theory a Modern Introduction*. Oxford University, 1993. ISBN: 0195076524.

[23] F. Petricca et al. "First results on low-mass dark matter from the CRESST-III experiment". In: *15th International Conference on Topics in Astroparticle and Underground Physics (TAUP 2017) Sudbury, Ontario, Canada, July 24-28, 2017*. 2017. arXiv: 1711.07692 [astro-ph.CO].

[24] Alexander L. Read. "Presentation of search results: the CL_S technique". In: *J. Phys. G* 28 (2002), p. 2693. DOI: 10.1088/0954-3899/28/10/313.

[25] Othmane Rifki et al. *Supporting Note for the ATLAS Vector Boson Fusion plus missing transverse momentum with 139 fb^{-1}*. Tech. rep. ATL-COM-PHYS-2019-1252. Geneva: CERN, Sept. 2019. URL: https://cds.cern.ch/record/2690779.

[26] Steven Weinberg. *The Quantum Theory of Fields VI,VII*. Cambridge University, 1995,1996. ISBN: 0521585554.